Chemical Engineering Journal 495 (2024) 153531

Contents lists available at ScienceDirect

Chemical Engineering Journal

journal homepage: www.elsevier.com/locate/cej

Sustainable cross-linked poly(glycerol–*co*–δ–valerolactone) urethane substrates and multipurpose transparent electrodes for wearable electronics

Pulikanti Guruprasad Reddy [a], Amit Barua [a], Timo Laukkanen [a], Bahar Mostafiz [a], Teija Tirri [b], Akseli Vainio [a], Vipul Sharma [a,*]

[a] Department of Mechanical and Materials Engineering, University of Turku, Turku 20500, Finland
[b] Faculty of Science and Engineering, Åbo Akademi University, Turku 20500, Finland

ARTICLE INFO

Keywords:
Sustainable substrates
Cross-linked poly(glycerol–co–δ–valerolactone) urethanes
Transparent conducing electrode
Stretchable sensors
Flexible electronics
Real-time human motion monitoring
Transparent flexible heaters

ABSTRACT

Substrates form the backbone of most flexible electronic devices. This study reports sustainable substrates based on a new class of cross-linked poly(glycerol-co-δ-valerolactone) urethanes for flexible and stretchable electronic devices. A cost-effective method is described for preparing these substrates via thermal cross-linking polymerization of poly(glycerol-*co*-δ-valerolactone) triol with diisocyanates on a glass mold. The developed substrates display high flexibility, stretchability (~673 %), transparency (~90 %), thermal stability (~300 °C), and degradability, essential for next-generation flexible devices. Using synthesized polymers as substrates, we develop stretchable transparent conducting electrodes (TCEs). An innovative fabrication technique involves applying a thin electrospun polyvinyl alcohol (PVA) nanofiber mat as wet film leveling agent to enhance the adhesion and even distribution of sprayed silver nanowires. Through heat and pressure-based nanowelding of silver nanowire junctions, we create TCEs with uniform conductivity, low sheet resistance (~40 Ω sq^{-1}), and good transparency (~70 %). To demonstrate the versatility of stretchable TCEs, we fabricated flexible devices like capacitive sensors, curvature sensors, strain sensors, and heaters. The TCE strain sensor exhibits low creep and consistent performance from 5–45 % strain, maintaining signal stability for over 200 cycles at 10 kPa. The fabricated pressure sensor responds to pressures from 0.5–300 kPa with a maximum sensitivity of 2.43 kPa^{-1} and stability for at least 2600 cycles. The curvature sensor shows increased capacitance at curvatures up to 600 m^{-1}. The flexible heater reaches 85 °C in under 10 s with 5.5 V and responds rapidly under 0–35 % strain. These devices effectively detect human motion, serving as wearable sensors and heaters in cold conditions, demonstrating real-life applicability.

1. Introduction

Flexible and wearable electronics have gained significant research interest given their diverse applications in soft robotics, human–machine interfaces, health technology, light–emitting diodes (LEDs), flexible displays, energy harvesting, energy storage devices, and other Internet of Things (IOT) [1–8]. Specifically, advanced wearable sensors are rapidly evolving due to their ability to conformal contact with human skin for real-time health monitoring [2,9]. These sensors transduce external pressure signals and human motions into electrical signals such as resistance, capacitance, voltage, and current for early detection and diagnosis of health conditions.

In this realm, various flexible sensors with different sensing mechanisms, such as capacitive, piezoresistive, piezoelectric, triboelectric, and optical sensing electronics, have been demonstrated [10]. The components within flexible sensors, especially substrates and active nanomaterials/polymers, play a crucial role in their development. Materials like metallic nanowires [11], carbon nanotubes [12,13], 2D materials [14], and conducting organic polymers [15] are extensively studied as active conducting parts. However, when compared to the improvisation of conducting layers and fabrication strategies reported, less attention is given to the development of flexible substrates. Although it is obvious that the substrates are foundational materials for wearable electronics, where they integrate all necessary active and passive components on their surfaces. For high–precision sensing and practical healthcare monitoring, the ideal flexible sensors require a comfortable substrate that should be soft, lightweight, capable of undergoing stretching, and bending, resilient to wear and tear, and ensuring conformal attachment

* Corresponding author.
E-mail address: vipul.sharma@utu.fi (V. Sharma).

https://doi.org/10.1016/j.cej.2024.153531
Received 9 April 2024; Received in revised form 24 June 2024; Accepted 25 June 2024
Available online 26 June 2024

to human skin [16–18]. Furthermore, when tailored for health monitoring and clinical uses, these substrates should exhibit high transparency and degradability. Such substrates are very valuable for manufacturing transient electronic devices aimed at implantable medical diagnostics and therapies [19,20]. These devices are designed to naturally degrade within the cellular environment post their operational lifespan, thus eliminating the need for secondary surgeries to remove them from the body. Nevertheless, conventional substrates such as silicon, glass, and metal-based substrates have limitations. They are not biocompatible, or sustainable, and do not meet the requirements of flexible substrates due to rigidity and brittleness, causing mechanical mismatches between the human skin so their transformation into a flexible form is challenging [21].

In pursuit of this goal, most wearable flexible sensors are fabricated from substrates based on commercially available stretchable polymers such as silicon-based elastomers (e.g. polydimethylsiloxane (PDMS), dragon skin, Ecoflex and sylgard), thermoplastic polyurethanes (TPU), and styrene–ethylene–butylene–styrene (SEBS) [16–18]. However, these materials are non-degradable [22] and contribute to electronic waste (e-waste) accumulation. Furthermore, they encounter additional hurdles; for example, silicon-based elastomers exhibit poor chemical resistance, leading to swelling in the presence of solvents [23]. Except for SEBS (~400 °C) [24], other stretchable substrates such as PDMS (~200 °C) [17], Ecoflex (~115 °C), [25] and TPU (~130 °C) [17] suffer from inadequate thermal properties. Additionally, the light transmittance of Ecoflex (72 %) [26] and TPU (80 %) [27] limit their use in the fabrication of flexible devices that require high transparency and high thermal stability. Therefore, there's a pressing need to explore and develop alternative substrates that not only address environmental concerns by being fully degradable post–use but also possess the needed properties for high–performance electronics.

In the current state of the art, a variety of sustainable flexible sensors based on natural materials such as plant-based materials [28,29] (e.g., wood, leaf–skeleton, pollen), and biopolymers [30–32](e.g., starch, cellulose, chitosan, silk, etc.), have been developed due to their abundance, robustness, and sustainability. During previous years, we have reported many leaf–skeleton–based sustainable electrodes [33] and tactile capacitive e-skins [34] and tested their applicability for real-time human motion monitoring. Some of these leaf–skeleton–based electrodes are also used as flexible heaters and thermography patches [35,36]. The unique microscale fractal patterns of the leaf skeleton enabled our capacitive e-skin sensors to achieve a sensitivity of 0.08 kPa^{-1}, effectively detecting pressure in the range of 0.007 to at least 60 kPa [34]. On the other hand, few degradable synthetic polymers such as poly(glycerol sebacate (PGS), poly(sebacoyl diglyceride)–graft–2–ureido–4[1H]–pyrimidinone (PSeD–U), poly(sebacoyl 1,6–hexamethylenedicarbamate diglyceride) (PSeHCD), dynamically covalently cross-linked elastomers (PFB), poly(octamethylene maleate (anhydride) citrate) (POMaC), poly(1,8–octanediol–*co*–citrate) (POC), poly(L–lactide–*co*–ε–caprolactone) (PLCL), urethane-based polymer (E–PCL), poly (lactic–*co*–glycolic acid (PLGA)), polycaprolactone (PCL), urethane-silk elastomers etc. reported as sustainable substrates in the literature for the fabrication of flexible sensors [37–42]. However, they often suffer from other wide range of problems like poor mechanical properties, transparency, sensitivity to environmental considerations, not maintaining sensitivity over wide pressure ranges, complicated fabrication procedures, etc. Thus, the development of sustainable methodologies for flexible substrate design combined with innovative fabrication procedures is crucial to create highly sustainable, transparent, and cost-effective flexible sensors for next-generation human health monitoring and human–machine interface devices.

In this study, we introduce a new class of sustainable elastomeric substrates made from cross-linked poly(glycerol–*co*–δ–valerolactone) urethanes, offering exceptional flexibility, stretchability, transparency, thermal stability, and degradability, ideal for flexible and stretchable devices. These substrates are synthesized easily through a simple and cost-effective process via thermal cross-linking polymerization of poly (glycerol–*co*–δ–valerolactone) triol with a variety of diisocyanates on a glass mold. For the fabrication of stretchable and transparent conducting electrodes (TCEs), we developed new methods to enhance conductive nanomaterial adhesion and distribution throughout the substrate surface. As part of these methods, a thin layer of PVA nanofibers was applied to the polymer film via electrospinning, serving as a temporary wet film leveling interface, followed by nanowelding of the silver nanowires (AgNWs) to fabricate mechanically robust and highly stretchable TCEs with uniform conductivity and low sheet resistance (~40 Ω sq^{-1} at decent transparencies, ~70 %). These stretchable TCEs, along with tactile sensors and thin film heaters fabricated with them, show excellent performance as wearables, detection of human motions, and rapid heating, promising a scalable and eco–friendly approach for advancing flexible electronics.

2. Materials and methods

2.1. Materials

All chemicals for the synthesis of polymer (glycerol, δ-valerolactone, stannous octoate, hexamethylene diisocyanate, 4,4′-methylenebis (cyclohexyl isocyanate), isophorone diisocyanate) and solvents (ethanol and dimethylformamide) were purchased from Sigma Aldrich and used as received without any purification. PVA (MW = 30,000–70,000 Da) for the electrospinning, AgNWs (70 nm x 40 μm) for the fabrication of stretchable TCE were also purchased from Sigma Aldrich. Cellulose tape for the fabrication of the capacitive sensor and Copper tape for the heater fabrication were purchased from 3 M.

2.2. Synthesis of prepolymer poly(glycerol–co–valerolactone) triol (1)

In a 100 mL round-bottom flask, glycerol (0.5 gm, 1 eq, 5.42 mmol), δ-valerolactone (6.68 gm, 12.3 eq, 66.78 mmol), and stannous octoate (71.8 mg, 0.01 wt% relative to the starting materials) were stirred and allowed to react under a nitrogen atmosphere at 130 °C for 24 h. After completion of the reaction, the stannous octoate in the reaction mixture was deactivated by adding 5 mL of methanol. The reaction mixture was then cooled to room temperature and purified by washing the resultant crude reaction mixture with diethyl ether (4 × 30 mL). A colorless and highly viscous solution of poly(glycerol-*co*-valerolactone) triol (1) was obtained in pure form after drying under high vacuum. This viscous solution was stored in a desiccator, and over time, it gradually solidified into a pasty white solid. Yield: 6.036 g (84 %). FT–IR (cm^{-1}) 3514, 3325 (ν O–H), 2991, 2960 (ν C–H), 1738, 1655 (ν C = O), 1414 (δ O–H), 1157, 1086 (ν C–O), 972, 903, 808, 714, 665 (δ C–H). ^{1}H–NMR (500 MHz, DMSO–d_6), δ 4.37 (s, 1H, glycerol–methine), 4.17 (dd, 2H, J = 11.1 Hz, glycerol–methylene), 4.01 (s, sharp peak, 12H, VL–methylene repeating chain), 3.38 (q, 2H, J = 5.45 Hz, VL–methylene end chain), 2.32–2.27 (m, sharp peak, 12H, VL–methylene), 1.57 (s, sharp peak, 24H, VL–methylene repeating chain), 1.42 (qu, J = 6.25 Hz, 2H, VL–methylene end chain). ^{13}C–NMR (125 MHz, DMSO–d_6), δ 173.37, 173.12 (C = O), 63.80 (glycerol–methine), 63.71, 60.70 (glycerol–methylene), 33.78, 33.42, 33.23, 28.0, 21.65, 21.49 (VL–methylene).

2.3. Synthesis of cross–linked poly(glycerol–co–δ–valerolactone) urethanes (S1–S3)

In a 10 mL glass vial, compound 1 (1 eq), diisocyanates (2 eq), and stannous octoate (3.5 wt%) were dissolved in 1.5 mL of dry DMF. The solution was gently mixed using a vortex for 2–3 min and then set aside for 10 min to allow bubbles in the solution to clear. Subsequently, the solution was drop-cast onto a glass mold (15 cm x 15 cm) and baked on a hot plate at 75 °C for 3 h. The glass mold was then cooled to room temperature, and the resulting cross-linked poly(glycerol-*co*-δ-valerolactone) urethane elastomers (S1-S3) were peeled off the mold after

cutting them to the required dimensions with a knife.

Following the general procedure, cross-linked poly(glycerol-*co*-δ-valerolactone) hexamethylene urethane (S1) was obtained as transparent and flexible films by reacting compound 1 (1 g, 0.755 mmol, 1 eq), hexamethylene diisocyanate (0.254 g, 1.55 mmol, 2 eq), and stannous octoate (44 mg, 3.5 wt%). FT–IR (cm^{-1}) 3370 (ν N–H), 2938, 2864 (ν C–H), 1720 (ν C = O), 1536 (δ N–H), 1453 (δ C–H), 1248(ν C–N), 1161, 1090, 1041 (ν C–O), 869, 826, 764, 739, 591.

Following the general procedure, the cross-linked poly(glycerol–*co*–δ–valerolactone) cyclohexyl urethane (S2) was obtained as transparent and flexible films by reacting compound 1 (1 gm, 0.755 mmol, 1 eq), 4,4′–methylenebis (cyclohexyl isocyanate) (0.396 gm, 1.511 mmol, 2 eq) and stannous octoate (48 mg, 3.5 wt%). FT–IR (cm^{-1}) 3371 (ν N–H), 2923, 2852 (ν C–H), 1724 (ν C = O), 1522 (δ N–H), 1454 (δ C–H), 1225 (ν C–N), 1160, 1090, 1035 (ν C–O), 979, 770, 739, 584.

Following the general procedure, the poly(glycerol–*co*–δ–valerolactone) isoprene urethane (S3) was obtained as transparent and flexible films by reacting compound 1 (1 gm, 0.755 mmol, 1 eq), isophorone diisocyanate (0.335 gm, 1.511 mmol, 2 eq) and stannous octoate (46 mg, 3.5 wt%). FT–IR (cm^{-1}) 3384 (ν N–H), 2953, 2875 (ν C–H), 1730 (ν C = O), 1538 (δ N–H), 1456 (δ C–H), 1248 (ν C–N), 1161, 1092, 1029 (ν C–O), 944, 860, 777, 745.

2.4. Fabrication of transparent conducting electrode (TCE)

In a standard procedure, the S2 substrate with dimensions of 3 cm x 3 cm was selected for the fabrication of the TCE. The surface of the substrate was coated with a nanofabric mesh of PVA layer using electrospinning techniques. A 15 wt% PVA solution in water was employed for electrospinning (Spinbox from bioinicia), applying a voltage of 22 kV and a flow rate of 2 μL/min in a 10 mL syringe. Subsequently, the PVA–deposited S2 is subjected to spraying of AgNWs (70 nm X 40 μm) at a concentration of 250 μg/mL in ethanol: water mixture (1:1 ratio) (2 mL) to make it conductive. The substrates were then nano welded at 120 °C for 20 min on a hot plate. Following this, the TCE substrates were allowed to cool to room temperature, and their resistivity was tested using a multimeter to confirm conductivity.

2.5. Characterization

The ^{1}H NMR and ^{13}C NMR spectra of prepolymer 1 were recorded using a Bruker 500 MHz spectrometer. The chemical shifts were reported as δ values (ppm) relative to the internal standard tetramethylsilane in DMSO-d_6. FT-IR spectra were recorded using a Bruker FTIR spectrophotometer (VERTEX 70). Thermogravimetric analysis (TGA) and differential thermal analysis (DTA) were performed using an SDT Q600 apparatus from TA Instruments under an N_2 atmosphere flow rate of 100 mL/min, with a heating rate of 10 °C/min from 25 to 600 °C. Contact angles of substrates were recorded using a Theta Optical Tensiometer with a sessile drop method. Transmittance studies of substrates were conducted in the wavelength region ranging from 250 to 1000 nm using a J.A. Woollam VASE ellipsometer. Stress–strain data of substrates were recorded using a texture analyzer (TA.XT.plus100C, Stable Micro System). High-resolution surface analysis of TCE was performed using an Apreo S field-emission Scanning Electron Microscope (SEM) (Thermo Scientific Inc., Eindhoven, The Netherlands) at 2 kV with an operating current of 25 pA. Elemental analysis was conducted using an EDS (Energy-Dispersive X-Ray Spectroscopy) attachment linked to SEM (Oxford Instruments UltimMax 100 EDS). The texture analyzer (TA.XT.plus100C, Stable Micro Systems) equipped with a cylindrical probe with a diameter of 20 mm was used to apply and vary the pressure on the capacitive pressure sensors. For the strain sensor, the same texture analyzer was equipped with a tensile grip to apply different stress–strain conditions for the device under test. The relative change in capacitance and resistance of both capacitive and strain sensors were measured using the LCR meter (GW-INSTEK LCR-6300). A testing signal of 1 V at 1 kHz was employed for all measurements on the LCR meter. The sheet resistance of the TCEs was measured using the Ossila four-point probe system (Product code: T2001A3), which features a probe spacing of 1.27 mm. for the heater experiment, the voltage was applied using a power supply (PeakTech 6225A). Infrared images were captured using FLIR One Pro infrared camera and the FLIR ETS320 integrated with the FLIR research studio.

2.6. Mechanical characterization

The stress vs strain profile of our substrates was measured using a standard mechanical tester, the TA.XT.plus100C from Stable Micro Systems. All the substrates were maintained at the same size of 1.5 cm x 1.2 cm (L x W) with uniform cross-sections, meeting the requirements for tensile test measurements according to the instrument's operating standard [43]. The testing procedure involves holding the sample between two grips set a fixed distance apart (15 mm). The force applied to the loading arm, attached to the top grip, moves upward at a constant speed until the sample undergoes deformation. During the test, the displacement by the probe (in meters), the applied force (in Newtons), and the time are all recorded in exponent. The stress and strain parameters of the substrates were calculated based on the following formulas:

$$\text{stress} = \frac{\text{force}}{\text{cross} - \text{sectional area}} \quad (1)$$

$$\text{strain} = \frac{\text{extension}}{\text{original length}} = \frac{\text{distance moved by top grip}}{\text{inital grip seperation}} \quad (2)$$

3. Results and discussion

3.1. Prepolymer synthesis, and characterization

The prepolymer, poly(glycerol–*co*–valerolactone) triol (referred to as compound 1 hereafter), is prepared using glycerol and δ–valerolactone as renewable starting monomers. These monomers possess non–toxic and degradable properties [44], making them ideal choices for prepolymer synthesis. By ring opening polymerization (ROP) of δ–valerolactone with glycerol in the presence of Sn(II)octate at 130 °C for 24 h under N_2, we have obtained pasty-solid compound 1 (Scheme 1a). Compound 1 is synthesized to incorporate it as a soft, degradable segment in the design process of flexible substrates. The ester and hydroxyl functionalities in the polymer backbone of 1 are potentially attractive options for fine-tuning the degradability and mechanical properties of a flexible substrate. The presence of ester linkages enables compound 1 to exhibit hydrolytic degradability, significantly contributing to the substrate's degradability properties. Meanwhile, the reactive hydroxyl groups in 1 are potentially suitable for chemical modifications to create homogeneous cross-linked polyurethane structures when reacted with monomers like diisocyanates (contributing to hard segments formation). This synergistic combination offers high flexibility, stretchability, thermal stability, transparency and degradability to the resulting substrates. Therefore, the preparation of compound 1 represents a versatile and environmentally responsible choice for polymer-based substrate design.

To confirm the functional groups in compound 1, Fourier Transform Infrared Spectroscopy (FT–IR) spectroscopy was employed. The formation of hydroxyl and ester functionalities 1 are confirmed by identifying major stretching frequencies for O–H, C = O, and C–O functionalities at 3514 cm^{-1}, 1738 cm^{-1}, and 1157–1086 cm^{-1} respectively (Fig. S1a, supporting information). Further, Nuclear Magnetic Resonance (NMR) spectroscopy was employed to characterize the organic functionality of compound 1. Integrations of NMR peaks of 1 as per its chemical structure is shown in Fig. S1b, supporting information. Compound 1 exhibits characteristic peaks for glycerol–methine and methylene protons (Ha, &

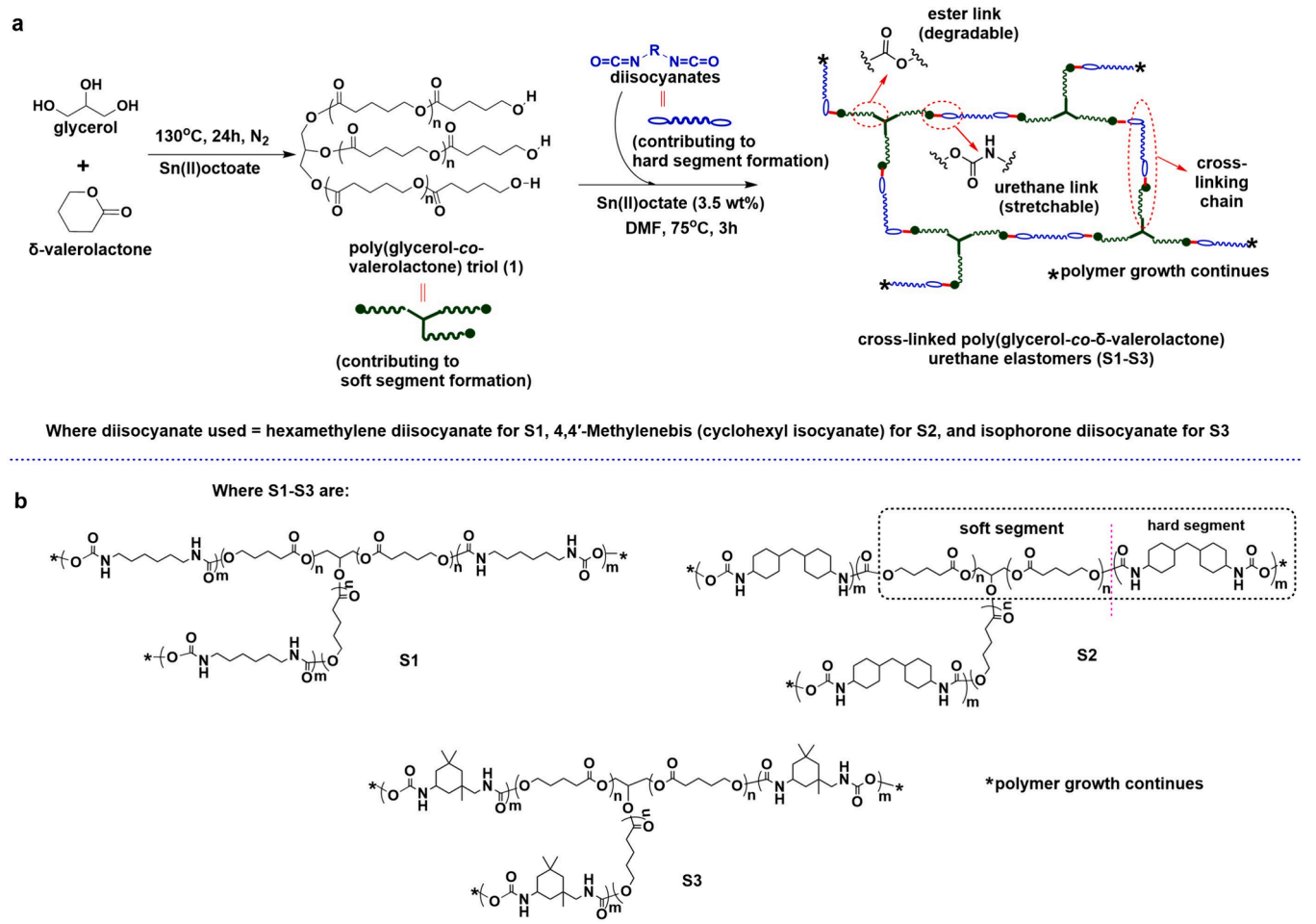

Scheme 1. Prepolymer synthesis and substrate design. (a) Synthetic route for cross–linked poly(glycerol–*co*–δ–valerolactone) urethanes (S1–S3). (b) Possible cross-linked chemical structures of S1–S3 substrates.

b) in the range of 4.37–4.14 ppm, confirming the formation of the tri–ester structure of glycerol in 1. Sharp NMR peaks noticed at 3.39 ppm for methylene protons in the end chain valerolactone (Hg) and at 4.01 ppm for methylene protons in the repeating valerolactone chain (Hc), confirm the occurrence of the ROP of valerolactone with glycerol. Additionally, sharp and highly intense resonance peaks were observed at 2.29 and 1.42 ppm, corresponding to the methylene protons Hd and He-f in the repeating valerolactone chain, respectively. This confirms the dense C–H functionality in the valerolactone chain of the prepolymer backbone (Fig. S1b, supporting information). Furthermore, the NMR of 1 is in good agreement with similar types of glycerol-based caprolactone polymers reported through the ROP process [45,46]. Based on the intensity of proton resonance signals of Hg and Hc, the number of repeating (n) units in 1 is established as 5.86. This gives the calculated number–average molecular weight (M_n) of 1 as 2152 g/mol. Additionally, to evaluate thermal properties, 1 was subjected to simultaneous TGA and DSC analysis (Fig. S1c, supporting information). 1 exhibits a crystalline nature, as evidenced by single melting temperature (T_m) [45] noticed in the DSC at 47 °C. TGA concludes that 1 remains stable up to 130 °C; however, decomposition begins thereafter, leading to a gradual weight loss reaching close to 100 % at a temperature of 300 °C.

3.2. Substrates design and characterization

To prepare a new class of cross-linked poly(glycerol-*co*-δ-valerolactone) urethane elastomers (S1-S3), we utilized the prepolymer (1), along with a variety of diisocyanates to form combinations of soft and hard segments, respectively (Scheme 1a &b). By varying the type of diisocyanate, such as hexamethylene diisocyanate, cyclohexyl diisocyanate, or isophorone diisocyanate during thermal cross-linking urethane reaction with prepolymer 1, we obtained a range of polymeric substrates, namely poly(glycerol–*co*–δ–valerolactone) hexamethylene urethane (S1), poly(glycerol–*co*–δ–valerolactone) cyclohexyl urethane (S2), and poly(glycerol–*co*–δ–valerolactone) isophorone urethane (S3) (scheme 1b). The diisocyanates offers improved mechanical properties to the resultant substrate due to the formation of a highly cross-linked urethane network with compound 1 hydroxyls (scheme 1a). To achieve homogeneous cross-linked polymeric substrates S1–S3 in a highly transparent, peelable, and free-standing form, we reacted prepolymer and diisocyanates in a 1:2 M ratio in the presence of DMF, tin(II) octoate catalyst on a glass mold for 3 h at 75 °C (Fig. 1a). The polymeric substrates produced using this facile approach demonstrated high transmittance and skin–like multifunctional properties including relaxing, stretching, twisting, bending, and conformal skin attachment, as shown in Fig. 1b. However, either decreasing or increasing diisocyanate concentration affects film properties due to non–homogeneity between the hard and soft segments. For example, when a high concentration of the diisocyanate (3 M ratios) was used, it resulted in substrates with poor transparency, while low concentrations (0.5 or 1 M ratios) resulted in un–peelable films, meaning no or poor formation of a cross-linked polymeric network. The easy and cost-effective approach developed here for the synthesis of cross-linked polymer elastomers on a glass mold is potentially useful for designing a variety of flexible substrates.

To identify the cross-linking ester–urethane network in substrates,

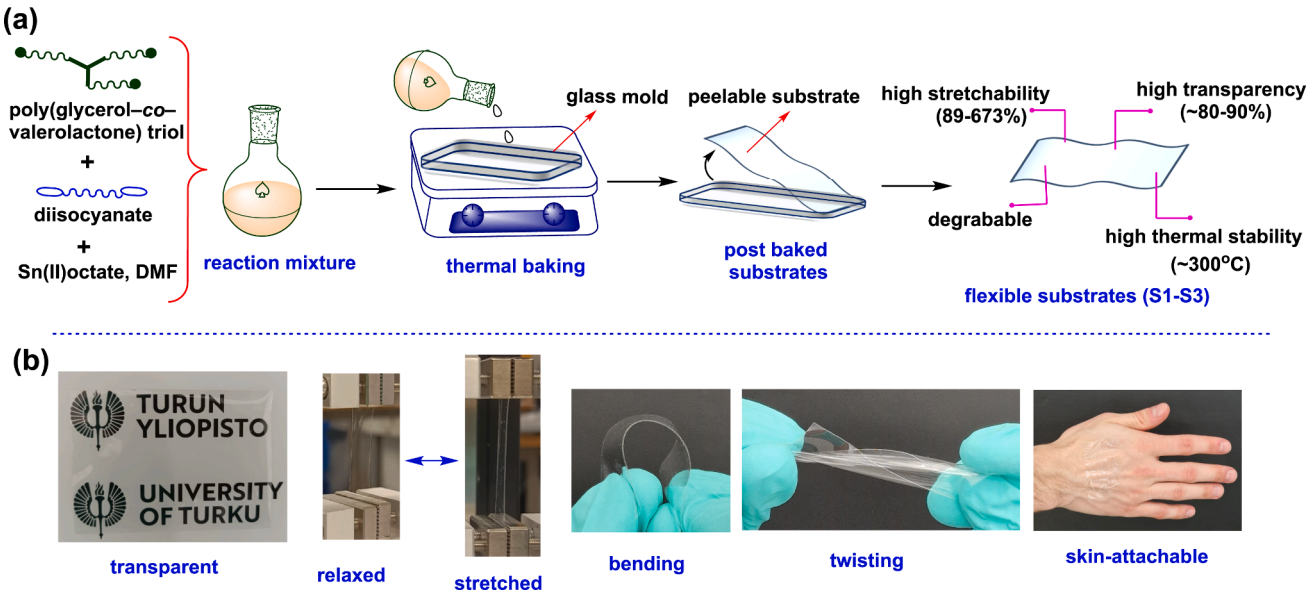

Fig.1. Substrates synthesis and properties. (a) Schematic Illustration of polymeric substrates S1–S3 synthesized on a glass mold. (b) Photographs of flexible substrate demonstrating transparency underneath the University of Turku logo, relaxed, stretched, bending, twisting, and conformal attachment to Human skin.

we subjected the developed substrates (S1–S3) to FT–IR analysis (Fig. 2a). The N–H, C = O, C–N, and C–O functionalities in the ester–urethane network of S1–S3 were identified by noticing the corresponding stretching vibrational frequencies in the ranges of 3370–3383 cm^{-1}, 1720–1730 cm^{-1}, 1225–1248 cm^{-1}, and 1160–1161 cm^{-1}. When compared with the O–H (3514 cm^{-1}) and C = O (1738 cm^{-1}) bond stretching frequencies in compound 1, the N–H (3370–3383 cm^{-1}) and C = O (1720–1730 cm^{-1}) stretching frequencies in substrates are lower in wavenumber shifted due to the ester–urethane network. This confirms the occurrence of the cross-linking reaction between compound 1 and diisocyanates. Additionally, the highly dense C–H functionality in the pendant chain of cross-linked polymeric substrates is identified by observing broad vibrational bands in the range of 2923–2953 cm^{-1}. The FT–IR data confirms the formation of a cross-linked ester–urethane network in substrates. However, due to the insolubility of substrates in organic solvents, their molecular structure characterization by NMR analysis is not accessed in the present work.

Further, to study the optical properties such as transmittance and reflectance, we conducted ellipsometry analysis for substrates S1–S3 (3 cm x 3 cm) in the wavelength region ranging from 400 to 800 nm. The substrates displayed high transmittance properties as revealed by the transmittance studies; whereas S1 and S3 displayed lower optical transparency around 80 % and 85 %, respectively, compared to S2, which exhibited the highest transmittance at approximately 90 %, as

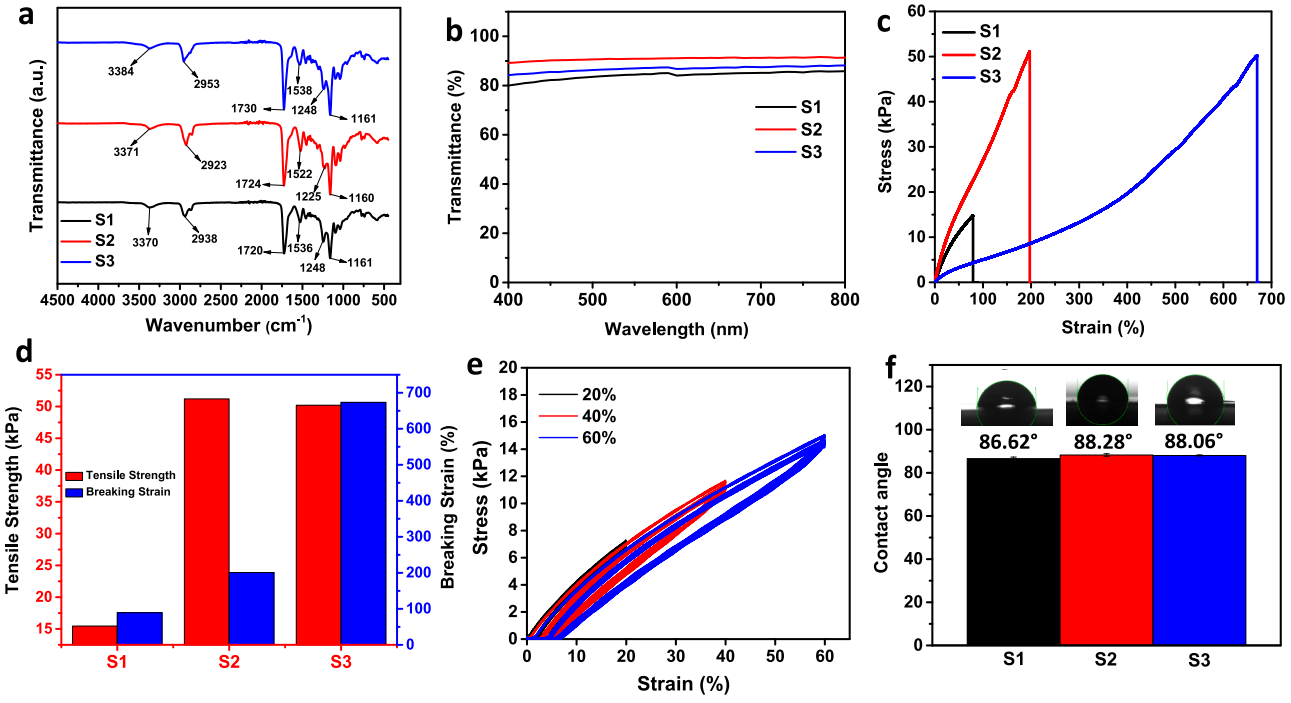

Fig. 2. Characterization data of S1–S3. (a) FT–IR data. (b) Transmittance data. (c) Stress vs strain data. (d) Tensile strength and breaking strain. (e) Stress vs strain data of S2 substrate at 20, 40, and 60% of strain for 5 cycles. (f) Static contact angles of water droplets on substrates S1–S3.

shown in Fig. 2b. These transmittance values did not change significantly even when the transmittance spectra were recorded at multiple angles by tilting the substrates, indicating homogeneous structural uniformity of substrates with the absence of surface defects or irregularities due to proper hard–soft segments combination. For example, the transmittance data of S2 recorded at different angles (15°, 30°, 45°, and 60°) show no change in transmittance, as depicted in Fig. S2, supporting information. Additionally, these substrates do not exhibit any reflectance, as confirmed by the reflectance studies, further indicating the smoothness and uniformity of substrates (Fig. S3, supporting information).

The mechanical properties such as tensile strength and breaking strain of the polymeric substrates S1–S3 were investigated using a mechanical tester. Samples, sized at 1.5 x 1.2 cm, were employed for strain–stress analysis. The results conclude that the breaking strain varies among the films. For example, S3 displayed the highest breaking strain at 673 % under a tensile strength of 50 kPa, in contrast to S2, which broke at 200 % strain with a nearly equivalent tensile strength of 51 kPa. Meanwhile, S1 exhibited a lower breaking strain of 89 % at a tensile strength of 15 kPa (Fig. 2c–d). Additionally, all these substrates displayed exceptional stretchability, retaining their original state without deformations even after a series of cyclic experiments at different applied strains. For example, Fig. 2e displays the stress–strain curves for S2 films tested at strains of 20 %, 40 %, and 60 % across 5 cycles, demonstrating their high stability and stretchability. The films returned to their original state without deformations and exhibited negligible hysteresis.

The highest breaking strain observed in S3 compared to S2 and S1 can be explained by their structure–property relationships. The tensile properties of urethanes are highly dependent on intermolecular hydrogen bonding, steric hindrance, and compatibility between the soft and hard segments [47,48]. Literature reports suggest that polyurethanes made with symmetric and non-sterically hindered hard segments can lead to high intermolecular hydrogen bonding, resulting in increased tensile strength and decreased strain properties compared to polyurethanes with asymmetric and sterically hindered hard segments [47]. Increased intermolecular hydrogen bonding restricts polymer chain movement, making the material stiffer and less flexible. Thus, breaking strain decreases, and toughness increases since the chains cannot extend as much under stress before breaking. In this study, the hexamethylene and bis-cyclohexyl urethane segments in S1 and S2 substrates are symmetric, displaying highly ordered intermolecular hydrogen bonding with soft segments due to the lack of steric hindrance. In contrast, the isoprene urethane segment in S3 is asymmetric and sterically hindered, resulting in poor intermolecular interaction between the soft and hard segments. This phenomenon is supported by observing slightly higher wavenumber shifts of N–H and C = O stretching frequencies in S3 at 3384 cm^{-1} and 1730 cm^{-1} can be due to poor or no hydrogen bonding interactions compared to S1 and S2 at 3370, 1720 cm^{-1} and 3371, 1724 cm^{-1}, respectively (Fig. 2a). The slight shift in N–H and C = O stretching frequencies is a significant observation in analyzing the structure–property relationship of polyurethanes [47–49]. Therefore, the high breaking strain of S3 is due to the poor or no hydrogen bonding nature caused by its asymmetric and sterically hindered hard segments, which allow the polymer chains to be more flexible, stretching to 673 % before breaking. On the other hand, the hydrogen bonding in S1 and S2, caused by symmetric and non-sterically hindered hard segments, makes the polymers more rigid and less flexible, resulting in lower breaking strains of 89 % and 200 %, respectively.

To evaluate the wettability characteristics of the designed substrates S1–S3, we conducted contact angle measurements. The results indicate that substrates S1, S2, and S3 displayed contact angles of 86.62°, 88.28°, and 88.06°, respectively (Fig. 2f). These values closely align with those typically associated with hydrophobic surfaces, falling within the range of 90–180°. The higher contact angles observed for the substrates suggest a limited presence of polar hydroxyl groups on their surfaces. This is likely attributed to involving the hydroxyl groups in the reaction with diisocyanate during cross-linking polymerization. As a result, the availability of polar hydroxyl groups for interaction with water droplets is less in number, which leads to an increase in the contact angles of substrates.

To assess the working thermal stability of the polymeric substrates S1–S3, we subjected them to testing on a hot plate up to 350 °C, with the temperature increasing steadily by 50 °C increments. These substrates demonstrated high thermal stability, maintaining their structural integrity up to approximately 300 °C on the hot plate, after which they began to undergo decomposition (Fig. S4, supporting information). Substrates with such elevated thermal stability are valuable for the fabrication of flexible devices required to operate at high temperatures in industries such as automotive, industrial manufacturing, the energy sector, aerospace, aviation, and beyond.

3.3. Transparent conducting electrode and flexible sensor fabrication

After the synthesis and characterization of substrates S1–S3, we chose substrate S2 as the model for fabricating the stretchable TCE. S2 was selected due to its high transparency and its convenient free-standing nature, making it easier to handle compared to substrates S1 and S3. The fabrication of TCE involves 3 steps that are illustrated in Fig. 3.

Wet film leveling is very important to achieve film uniformity to eliminate any surface irregularities and achieve uniform conductivity throughout the surface. When NWs or any NW-based inks are sprayed on the surface, it typically requires wetting agents or leveling additives to achieve uniform spreading. To achieve the wet film leveling and uniform deposition of the nanowires, we introduced a new nanofiber-based method. In the first step, a very thin layer of PVA nanofibers was electrospun on the prepared polymer film. The details of the electrospinning parameters are given in the experimental section. As evidenced from the SEM micrographs in Fig. 4a, a very thin layer of PVA nanofibers (average diameter ~ 43 nm) is uniformly deposited on the surface. This PVA layer acts as the underlying leveling layer due to the pores and higher surface area of the nanofibers.

In the second step, high aspect ratio AgNWs (70 nm x 40 μm) at an optimized concentration of 250 μg/mL in ethanol: water mixture (1:1) were sprayed onto the PVA–coated S2. Due to the underneath super hydrophilic wetting layer of PVA, the AgNW solution in the ethanol: water mixture quickly spread on the surface making a uniform layer, covering the whole surface. On the other hand, the wetting of the control surface (without PVA coating) was uneven as evidenced by Fig. S5, supporting information. The spray comes as numerous small droplets of the NWs in solution. The schematic in Fig. 3 shows how ethanol: water mixture droplets spread across the surface of electrospun nanofibers due to capillary and viscous frictional forces. When ethanol: water mixture is sprayed onto the nanofiber surface, it quickly moves across the fibers,

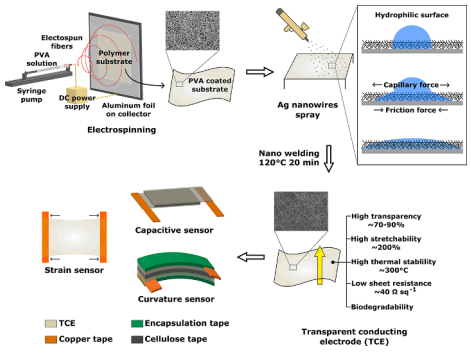

Fig.3. Pictorial representation for the fabrication process of TCE and layout of a strain sensor, capacitive pressure sensor, and curvature sensor.

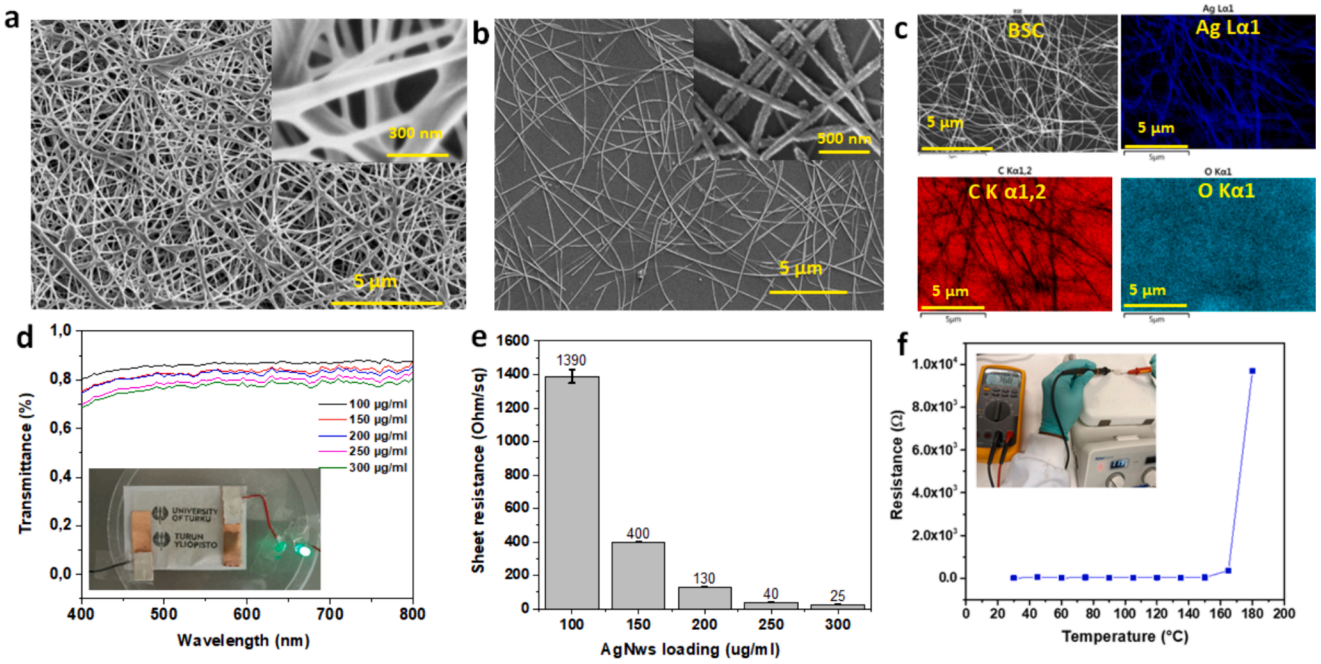

Fig.4. TCE characterization. (a) SEM micrographs of electrospun PVA fabric network on S2 (inset showing high-resolution SEM micrographs of PVA fiber network on the substrate). (b) SEM image of AgNWs across the TCE (inset showing high-resolution SEM image of nano welded AgNWs on S2). (c) backscattered electrons for AgNWs network across TCE and corresponding EDS for silver, carbon, and oxygen elements in TCE. (d) Transmittance data of TCE fabricated with different concentrations of AgNWs (100, 150, 200, 250, 300 µg/mL) (inset: TCE loaded with 250 µg/mL AgNWs shows transparency with underneath of University of Turku logo along with blowing LED. (e) sheet resistance data of TCE fabricated with different concentrations of AgNWs (100, 150, 200, 250, 300 µg/mL). (f) resistance vs temperature profile of TCE.

spreading out from top to bottom (Fig.S5, supporting information). This phenomenon happens because the nanofibers have a large surface area, which increases the pressure gradient. As a result, tiny droplets of ethanol: water mixture spread and wet the surface as soon as they land. Then, a layer forms on the surface, helping the droplets to spread even faster. We see complete spreading, indicating strong adhesion forces. This spreading is due to a balance between capillary forces, which pull the droplet outwards, and viscous frictional forces, which resist this movement. When the fibers are very small, viscous forces become stronger than capillary forces. However, our observations of efficient and complete wetting suggest that the nanofiber mat has the right size and spacing to allow capillary forces to be more influential than viscous forces.

The third step involves the nanowelding of the NWs. Nanowelding is crucial for enhancing electrical conductivity, mechanical stability, improved durability, and efficiency [50,51]. For this purpose, the film obtained in step 2 was placed on a hot plate at 120 °C and a pressure of ~ 10 kPa was applied for 20 min. The junctions of the nanowelded NWs with an average diameter of ~ 70 nm can be seen in Fig. 4b. This step ensures stable electrical performance of the resultant TCE by lowering the resistance at the junctions of the AgNWs due to welding. Additionally, the nano welding process also has high adhesion of AgNWs to the substrate with enhanced mechanical properties during stretching and bending operations. The average sheet resistance of the TCE (with 250 µg/mL AgNWs loading) before nanowelding was 200–500 Ω sq^{-1} while after the nanowelding, it dropped to 40 Ω sq^{-1}. It is noteworthy to mention that the PVA layer acts as a temporary leveling layer on the substrate as it disappears after the deposition of AgNWs (Fig. 4b and Fig. S5, supporting information). Further, to confirm the AgNW distribution on the TCE, the energy–dispersive X-ray spectroscopy (EDS) measurements were performed. The EDS images are shown in Fig. 4C, which confirms the presence of AgNWs distributed on the surface of the TCE along with C, and O elements (Fig. 4c).

The effect on the optical and electrical properties of TCE by varying the concentrations of AgNWs was studied. For this purpose, TCEs loaded with AgNWs concentrations of 100, 150, 200, 250, and 300 µg/mL were fabricated and tested. The transmittance properties of TCEs are influenced by the amount of AgNWs loading. TCEs exhibited a slight decrease in their transmittance with an increase in silver loading from 100–300 µg/mL, as illustrated in Fig. 4d. For example, TCEs loaded with the highest AgNWs concentration (300 µg/mL) displayed a transmittance of nearly 70 %, which is 10 % lower compared to TCEs loaded with the lowest AgNWs concentration (100 µg/mL) at 80 %. However, when compared to the transmittance of TCEs loaded with the highest AgNWs concentration (300 µg/mL) to the neat substrate S2 (without silver loading, Fig. 2b), the transmittance is significantly reduced by 20 %. This decrease in transmittance of TCEs can be attributed to the presence of metallic silver exhibiting high light scattering [52,53]. Notably, even with a high silver loading (300 µg/mL), the fabricated TCEs maintained reasonable transmittance (~70 %) and a highly conductive surface (with a low sheet resistance of ~ 25 Ω sq^{-1}), making them suitable for transparent flexible electronics.

On the other hand, an increase in the conductivity of TCEs is observed with higher AgNW loading (Fig. 4e). For example, TCEs exhibited an average sheet resistance of 1390 Ω sq^{-1} when loaded with AgNWs at a concentration of 100 µg/mL. In contrast, the sheet resistance significantly decreases to 40 Ω sq^{-1} and 25 Ω sq^{-1} when the AgNWs loading increases to 250 µg/mL and 300 µg/mL, respectively. This reduction in sheet resistance is attributed to the increased density of AgNWs on the substrate surface, as confirmed by SEM analysis. SEM images in Fig. S6a–b (supporting information) show a lower distribution density of AgNWs in TCEs fabricated with 250 µg/mL AgNWs compared to those loaded with 300 µg/mL AgNWs. These results demonstrate that the conductivity of TCEs can be adjusted by varying the concentration of loaded AgNWs. Furthermore, the effect of temperature on the resistance of TCE was investigated (Fig. 4f). To this end, the TCE, which initially displayed a resistance of 40 Ω at an AgNWs loading of 250 µg/mL, was utilized. The findings indicate that the sheet resistance of TCE remains

relatively stable up to 160 °C. However, a sudden increase in resistance observed beyond 160 °C can be due to heat-induced degradation and fusion of the AgNWs [54–56]. These findings suggest that the fabricated TCEs demonstrate thermal stability by maintaining consistent conductivity up to at least 160 °C, making them suitable for high–temperature–stable flexible devices.

The strain effect on the conductivity of the fabricated TCE was investigated using a texture analyzer in combination with an LCR meter. The TCE having an initial resistance of 40 Ω sq^{-1} was subjected to varying strains from 5-45 %. The TCE showed a minimal change in resistance from 40 Ω sq^{-1} to 75 Ω sq^{-1} at low strain conditions (5–10 %) and reached a maximum of 460 Ω sq^{-1} at an applied strain of 45 % (Fig. S7, supporting information). However, the resistance reverted to its initial value once the strain was released. Due to stretching, the AgNWs on the substrate became more oriented along the direction of the applied strain. This orientation can lead to an increase in the junction resistance between the AgNWs, resulting in higher resistance of the TCE. When the strain is released, the AgNWs reorient themselves back to their original configuration, thereby reducing the junction resistance and returning the TCE to its initial performance [57]. These studies conclude that our TCE exhibits good tolerance and mechanical robustness towards strain, making it suitable for stretchable devices.

To confirm the adhesion stability of AgNWs on the TCE, we performed a Scotch tape test and repeated the test for 5 cycles. The tape was applied to the TCE surface and peeled off after 10 s, and the relative change in resistance was measured using a LCR meter with four-point probe. As shown in Fig. S8, supporting information, the initial resistance of the TCE before applying the tape was ~ 40 Ω sq^{-1}. This resistance increased to ~ 54 Ω sq^{-1} after the 1st cycle and reached a maximum of ~ 104 Ω sq^{-1} after the 5th cycle. The gradual increase in sheet resistance was due to the partial loss of AgNWs on the TCE surface. This indicates that most of the AgNWs remained strongly adhered to the substrate, as the TCE maintained homogeneous conductivity throughout the TCE even after the 5th cycle of the tape test. This indicates reasonable adhesion of AgNWs to the TCE surface.

Further, the properties of the TCE (40 Ω sq^{-1}) were studied under various mechanical deformations such as relaxed, bending, twisting, crumpling, and stretching conditions using the TCE as a conductor in a circuit to power an LED at 3 V. The studies concluded that the conductivity of the TCE is not affected by bending, twisting, and crumpling conditions, as these deformations displayed a similar intensity of LED brightness compared to the relaxed TCE (Fig. S9 a-d, supporting information). However, the conductivity of the TCE changes when strain is applied. The LED showed a visible decrease in brightness when the TCE was stretched to 30 %, indicating a decrease in conductivity, and the LED brightness returned to its original intensity when the strain was released (Fig. S9 e-f and video S1, supporting information). The decrease in TCEs conductivity in stretched conditions was due to the increase of resistance (Fig. S7, supporting information). These studies indicate that our TCE is flexible and robust, maintaining its conductivity under various mechanical deformations, though it exhibits a reversible change in conductivity when stretched. This demonstrates the potential of our TCE for applications in flexible and stretchable electronic devices.

After the fabrication and characterization of the TCE, its applicability and versatility were demonstrated by fabricating a variety of flexible and stretchable tactile sensors, including a strain sensor, capacitive pressure sensor, and curvature sensor as illustrated in Fig. 3. For this purpose, TCE with an average sheet resistance of approximately 40 Ω sq^{-1} was utilized for the fabrication of these flexible sensors. The strain sensor is fabricated by attaching conductive copper tape to both ends of the TCE, enabling precise measurement of mechanical strain. The pressure sensor is fabricated by sandwiching a layer of single side transparent cellulose tape between two TCE substrates, where the cellulose tape serves as a dielectric layer. Subsequently, the curvature sensor is derived from the capacitive pressure sensor by applying encapsulation tape on either side of the pressure sensor. This approach ensured the versatility and efficacy of the TCE, making it suitable for various flexible and stretchable devices.

The performance of the strain sensor was tested by measuring real-time resistance change ($\Delta R/R_0$) in response to applied strain using a combination of an LCR meter and a mechanical tester, respectively. Strain studies were conducted with strains ranging from 5–45 % with a constant increase of 5 % for each interval and each applied strain was tested for 5 cycles. The sensor showed an increase of $\Delta R/R_0$ response with the increase of applied strain ranging from 4–45 %, as shown in Fig. 5a. The sensor can withstand strains up to 45 % and shows minimal creep in $\Delta R/R_0$ change and repeatability. However, beyond a 45 % strain, the sensor begins to exhibit inconsistency in $\Delta R/R_0$, likely due to crack–based failure of AgNWs on the TCE surface [58,59]. Further, to assess the device's stability, the sensor was subjected to stretching – releasing cycles at a 10 % strain. As shown in Fig. 5b–c, the $\Delta R/R_0$ change remains stable for 200 cycles, indicating the repeatability and stability of the strain sensor. Based on these results, we conclude that our strain sensor exhibits a robust response to changes in $\Delta R/R_0$ under varying applied strains (5–45 %), potentially suitable for real-time monitoring of various human motions such as bending of fingers, wrists, arms, knees, etc.

The performance of the fabricated capacitive sensor was studied by measuring the relative change in capacitance ($\Delta C/C_0$) under varying pressure (P) in the range of 0.5–300 kPa. The pressure range measured herein typically covers the low (0–10 kPa) to higher pressure levels (100–300 kPa) experienced by human skin during normal activities [60]. A mechanical tester equipped with a cylindrical probe (20 mm diameter) was used to incrementally increase the pressure from 0.5–300 kPa on the active area of the sensor, and its relative capacitance $\Delta C/C_0$ change was recorded using an LCR meter. To assess the repeatability of relative capacitance, five cycles were recorded at each applied pressure. As shown in Fig. 6a, the $\Delta C/C_0$ of the sensor increases with the increase of applied pressure ranging from 0.5–100 kPa. This observed change is due to varying the distance between the working electrodes of the sensor as the pressure increases. Furthermore, the relative change of $\Delta C/C_0$ as a function of applied pressure is presented in Fig. 6b. A significant number of data points were collected below 10 kPa to check the $\Delta C/C_0$ change at the low–pressure region, as shown in the inset of Fig. 6b. To comprehensively assess the sensor's dynamic properties, including drift, capacitance change stability, and repeatability, we conducted cyclic tests. This involved subjecting the sensor to dynamic testing under low–pressure conditions of 20 kPa, with a frequency of 0.13 Hz, repeated for 2600 cycles. As shown in Fig. 6c, the sensor exhibited slight variations in signal intensity initially, suggesting minimal drift; however, overall device performance remained stable and repeatable over extended cycles. The magnified signal intensity of the pressure sensor in Fig. 6c illustrates its stability under constant pressure conditions.

Based on the data from Fig. 6a–b, we plotted the sensitivity of the sensor as a function of the applied pressure, as shown in Fig. 6d. Calculating sensor sensitivity is crucial for understanding the device's performance under applied pressure conditions. We calculated the sensitivity (s) of the fabricated sensor based on the following equation: [34]

$$S = \frac{d\left(\frac{C}{Co}\right)}{dP} \tag{3}$$

Where: C is the capacitance, C_0 is the initial capacitance, d is the distance between the working electrodes, and P is applied pressure.

As depicted in Fig. 6d, the maximum sensitivity of 2.43 kPa^{-1} is observed for the sensor in the pressure region of 0.5–100 kPa. Beyond 100 kPa, the sensor sensitivity experiences a sharp decline and no significant enhancement in $\Delta C/C_0$ is noticed after 300 kPa. Exceeding the sensor's maximum measurable pressure value may cause failure in hard or rigid electronics, but in flexible devices, sensitivity decreases

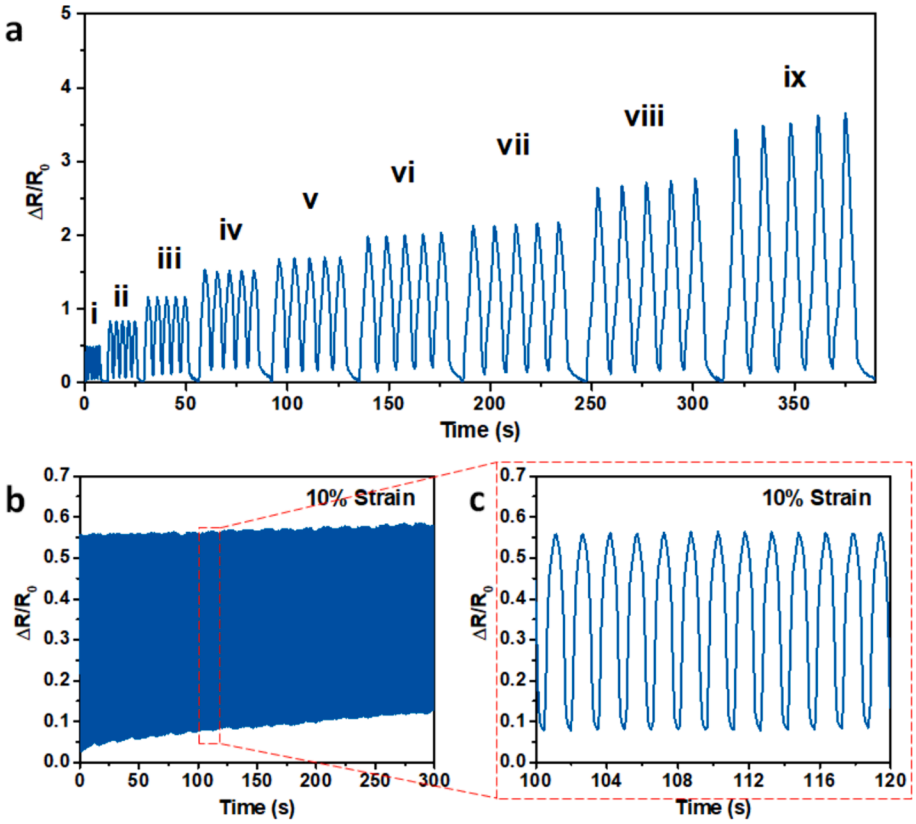

Fig. 5. Strain sensor data. (a) Strain sensor shows change in the $R–R_0/R_0$ with increase of strain from 5–45 % (i = 5 %, ii = 10 %, iii = 15 %, iv = 20 %, v = 25 %, vi = 30 %, vii = 35 %, viii = 40 %, ix = 45 %). (b) Stability of the strain sensor shows when stretched dynamically for 200 cycles under applied strain of 10 %. (c) Magnified image from (b) showing the change in resistance with the corresponding strain cycles.

gradually with rising pressure.

It is noteworthy to mention that the linearity and sensitivity of capacitive sensors depends on several factors, including the dielectric constant and type of the dielectric layer, microstructures on the dielectric layer, type of electrode, and air gaps within the dielectric layer [61,62]. To further enhance sensor linearity, we fabricated and tested the sensor using another design of dielectric layer where we used two layers of double-sided cellulose tape as dielectric, compared to the design shown in Fig. 3, which used single-sided cellulose tape as the dielectric layer. This architecture leads to improved linearity when compared to the former case, tested under similar pressure regions of 0.5–300 kPa (Fig. S10, supporting information). Changing the device architecture from single-sided to two layers of double-sided cellulose tape improves air gaps between the dielectric layer, thereby enhancing the sensor's linearity.

The pressure sensor also serves as a curvature sensor upon encapsulation of degradable cellulose tape on both sides (Fig. 3). This protective measure prevents electrode stretching while preserving flexibility for bending the sensor on curved surfaces. To assess its performance, the sensor was tested by clamping its edges on a linear translation stage and applying bending force to curve it from 0–600 m^{-1}. Simultaneously, the corresponding relative change in $\Delta C/C_0$ was recorded using an LCR meter. This rigorous testing procedure was repeated four times, and the results were averaged to obtain a reliable calibrated capacitance profile as shown in Fig. 6e. The curvature of the sensor was precisely calculated from its bending images using the Image J software. The results show that a quadratic relation of $\Delta C/C_0$ change is observed with an increase in curvature spanning from 0–600 m^{-1}. These findings affirm the efficacy of the fabricated curvature sensor in effectively monitoring capacitance in curved areas, highlighting its versatility and reliability in real-world applications.

Benefitting from the capacitive sensor's high sensitivity, stable response, and cyclic stability under applied different pressures, we demonstrated its applicability in the real-time monitoring of human activities. Various types of human body motions such as finger movement, wrist movement, vocal cord vibrations, etc., were monitored by attaching sensors to the body. Monitoring such human activities in real-time is crucial in health technology [63,64]. Using a capacitive sensor, we fabricated a smart wearable nitrile glove for finger gesture monitoring. The smart glove fabrication involves mounting a capacitive sensor on each finger of the glove. The sum capacitance of these sensors on a smart glove was maintained for gesture monitoring by connecting them in a parallel manner. The sum capacitance for smart glove is calculated using the following equation (2).

$$C_{Total} = C_1 + C_2 + C_3 + C_4 + C_5 \quad (4)$$

A series of finger gestures were performed, with each gesture being maintained for 15 s. The fabricated smart glove can detect the gesture movement of fingers, where it displays stable and repeatable $\Delta C/C_0$ change in the action of pressure created by finger gesture as shown in Fig. 7a. The capacitive sensor mounted on the human wrist displayed consistent patterns of capacitance change in real-time response to wrist movements, as illustrated in Fig. 7b. Furthermore, the capacitive sensor is utilized to detect various human vocal activities such as speaking, laughing, and swallowing by positioning the sensor on the throat. In Fig. 7c, changes in capacitance ($\Delta C/C_0$) are displayed for different vocal activities, including swallowing, and speaking, in comparison to normal conditions. These demonstrations suggest that the developed sensor holds promise for monitoring both high and low–pressure human body motions in real time. This real-time monitoring is particularly advantageous in the medical field for health monitoring devices and other applications, including voice input signal detection.

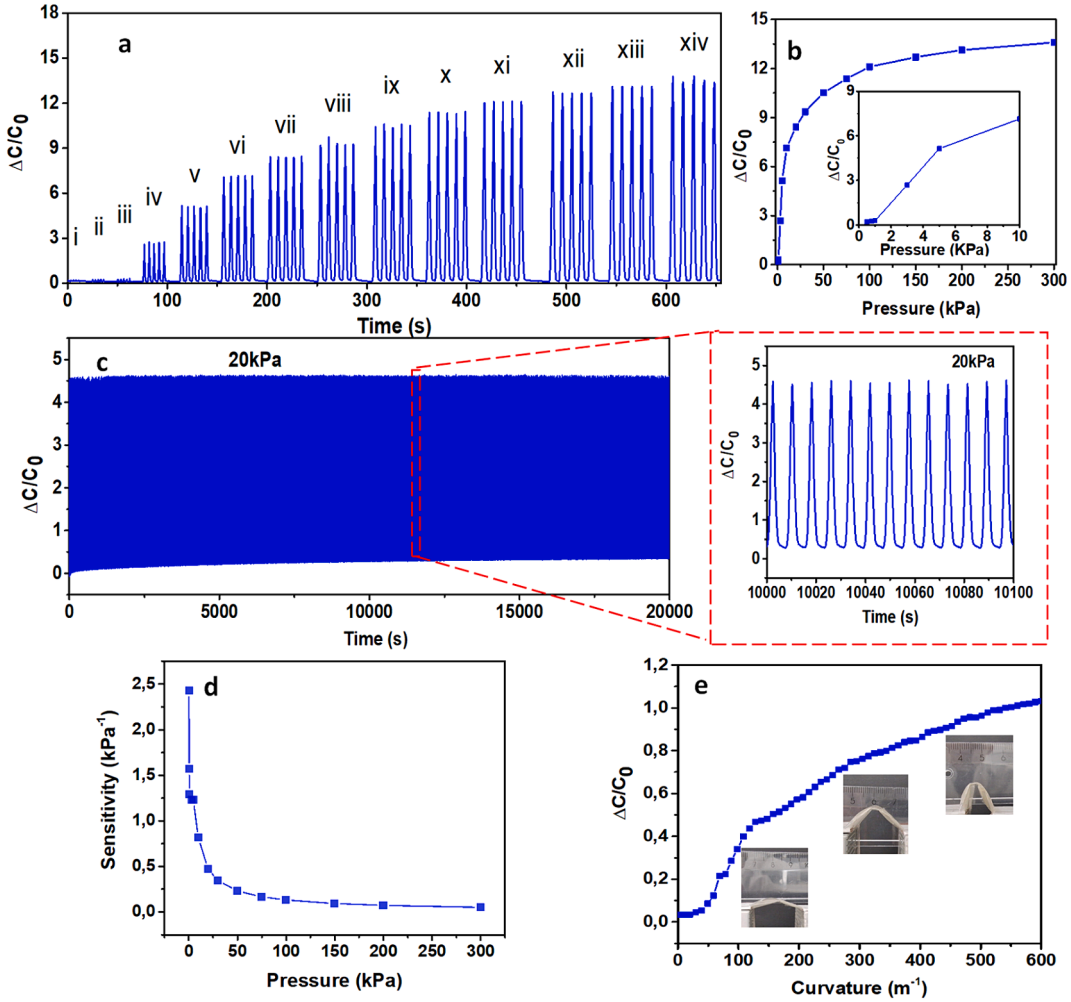

Fig. 6. Capacitive and curvature sensor characterization. (a) Displays the variation of $\Delta C/C_0$ with the applied pressure on the sensor ranging from 0.5–300 kPa (where i = 0.5 kPa, ii = 0.8 kPa, iii = 1 kPa, iv = 3 kPa, v = 5 kPa, vi = 10 kPa, vii = 20 kPa, viii = 30 kPa, ix = 50 kPa, x = 75 kPa, xi = 100 kPa, xii = 150 kPa, xiii = 200 kPa, xiv = 300 kPa), (b) shows relative capacitance plotted as a function of pressure. Inset showing the close–up of pressures below 10 kPa. (c) Shows the stability of the capacitive sensor when dynamically loaded for 2600 cycles with a pressure of 20 kPa. The stability in capacitance change is depicted in the magnified image. (d) Shows the calculated sensitivity derived from the data in (a &b), (e) Curvature sensor showing the relative change in capacitance ($\Delta C/C_0$) with applied curvature 0–600 m^{-1}.

3.4. *Flexible heater fabrication and testing*

To demonstrate the application of the fabricated TCE as a flexible heater, we studied its Joule heating characteristics. For this purpose, stretchable TCE (3 cm x 2 cm) with an average sheet resistance ~ 40 Ω sq^{-1} (AgNWs loading at 250 μg/mL) was used as a transparent and flexible heating surface. The fabrication of the flexible heater involved connecting copper tapes on both ends of the TCE, as depicted in Fig. S11, supporting information. The data and thermal images of the TCE heater were recorded using FLIR thermal studio.

To study the heating characteristics, a continuous DC voltage was applied to the heater increasing from 0.5 V to 6.0 V (with 0.5 V increment) every 60 s until the heater failed (Fig. 8a). As the voltage across the heater increased, the steady–state saturation temperature increased monotonously. As can be seen in IR images of Fig. 8a, the heater exhibited uniform heat distribution across the surface with the increase in applied voltage, demonstrating the even distribution of AgNWs. The heater remains stable up to an applied voltage of 5.5 V at an average heater temperature of 85 °C. However, it failed when reached the highest average temperature of 90 °C at the applied voltage of 6 V. The failure was likely due to the high local temperature causing the snapping of the silver nanowires[57] at certain points of the heater joints connected with external copper tape. The snapping of the AgNWs on the TCE was caused by local heating rather than the applied voltage. This assertion is supported by the observed increase in TCE sheet resistance due to the snapping of the AgNWs with the rise in externally applied heat as shown in Fig. 4f.

To assess the response time and reliability of the TCE heater, we recorded the time-dependent temperature profile by testing at different applied voltages ranging from 0.5 V to 3.5 V (Fig. 8b) with constant applying voltage–on for 60 s. As evident in Fig. 8b, the surface temperature of the heater increased almost instantaneously with their corresponding ramping applied voltages and reached their steady–state operating temperature within ~ 10 s. Additionally, Fig. 8b indicates that the heater can maintain a steady–state temperature continuously when the voltage is applied and shows a sharp decline in temperature when the voltage is turned off. Furthermore, we assessed the repeatability and performance of the TCE heater by testing the voltage on and off at repeated time intervals (15 s) for 10 cycles at different voltages (0.5 to 3.5 V) as depicted in Fig. 8c. The results revealed that no significant change in heater surface temperature or response time was observed when the heater was turned on and off at repeated intervals, indicating its repeatability and reliability. The stretchable TCE-based heater shows uniform heat distribution, with a rapid heating and cooling response.

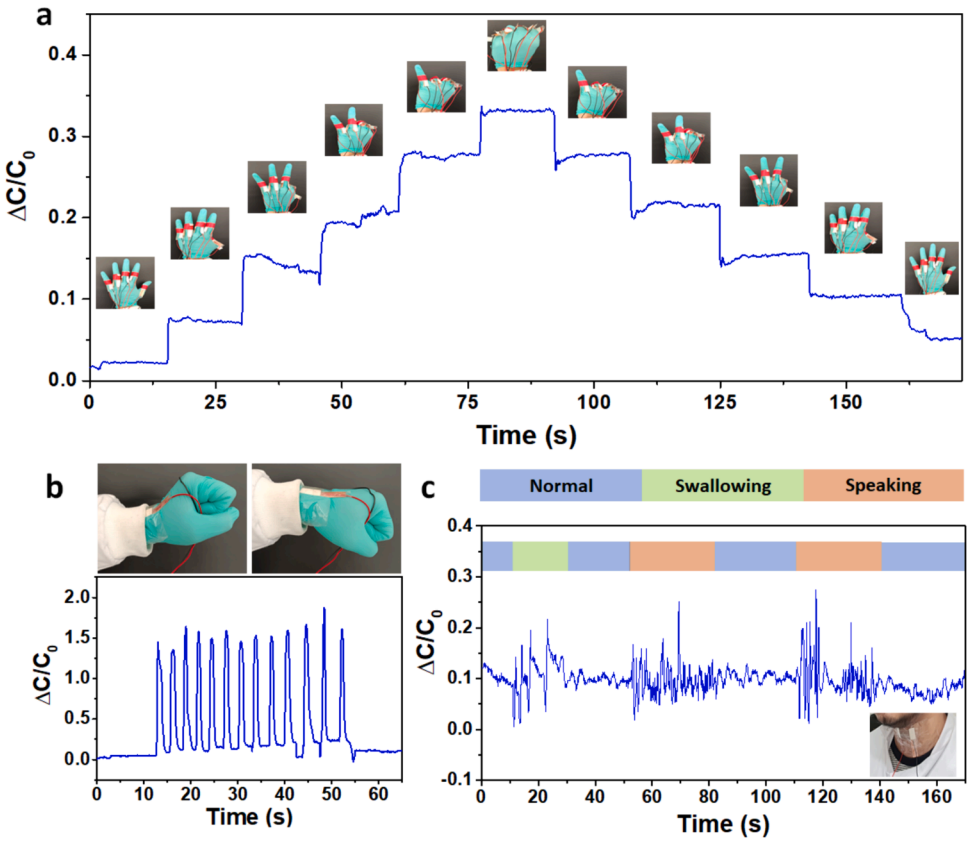

Fig. 7. Demonstration of capacitive sensor for gesture monitoring. (a) Smart glove shows the stable and distinguishable $\Delta C/C_0$ change for different finger gesture movements. (b) The capacitive sensor mounted on the hand wrist shows repeatable $\Delta C/C_0$ changing patterns for wrist movement. (c) Capacitive sensor shows $\Delta C/C_0$ change for different vocal cord vibrations speaking, swallowing, etc.

This is due to the high surface area of the AgNW in addition to the substrate's low thermal mass characteristics that are typical for film heaters following the Joule heating principle. Furthermore, the substrate exhibits excellent thermal stability up to ~ 300 °C, electrical insulation properties, and superior mechanical integrity with conducting AgNWs tolerance up to 45 % of strain, making the heater highly robust and suitable for various applications, including automobiles, medical, aerospace, and consumer electronics.

Further investigation into the heating characteristics of the flexible heater was conducted under increasing strain conditions. Strain was incrementally applied to the heater from 0 % to 35 % (in 5 % increments every 60 s) at a maximum applied bias of 5.5 V. The results indicated that the heater's maximum temperature, approximately 95 °C under no strain, significantly dropped to 32 °C at 35 % strain. Upon releasing the strain, the heater returned to its maximum temperature of around 95 °C as evidenced in Fig. 8d. Infrared camera images showing the change in heating with applied strain are presented in Fig. S12 (supporting information). Additionally, a video (Video S2) showing the heater under 20 % strain and corresponding change in heating is included in the supplementary information. The observed decrease in heating under stretching conditions is due to the increased resistance of the TCE, caused by higher junction resistance between the AgNWs as they align with the applied strain [57]. Once the strain is released and the AgNWs return to their original positions, the resistance decreases, resulting in higher heating. These findings demonstrate that the prepared heater is highly flexible and can effectively serve as a stretchable heating element with adjustable temperatures.

Additionally, to assess the stability of AgNWs on the heater, we conducted heating experiments on a heater that had been stored at room temperature for two months. The results revealed that the heater exhibited similar heating performance when compared to a freshly prepared heater, even after two months of aging (Fig. S13, supporting information). These findings indicate that the conductive AgNWs network on the heater remains stable for at least two months, demonstrating good stability.

The transparent heater, utilizing the stretchable TCE, was tested under real-life conditions, particularly in extremely cold environments. The demonstration was conducted in an outdoor environment at temperatures of –11 °C. A standard power bank (rated: power 37 W, voltage 5 V and maximum current 2.1 A) along with a controlled output voltage regulator (rated: power 3.5 W, operating voltage 5 V and 3.3 V, maximum current 0.7 A) was connected to the heater mounted on a diecast toy. In Fig. 8f, the IR image displays measured temperatures of the outdoor environment (–11.3 °C) and the toy surface (–6.6 °C) during the heater's off–state. While the heater was turned on, the temperature of the surface increased from –6.6 °C to 30 °C as shown in Fig. 8g, demonstrating its potential stability and capabilities to operate in very low–temperatures. The surface temperature of the heater can be adjusted, allowing it to serve both as a transparent thermotherapy patch for healthcare and for defrosting applications in extremely cold conditions.

3.5. Degradability studies

To evaluate the degradability of the S2 film used in TCE fabrication, we studied its degradation properties over 145 days. The studies were conducted in various aqueous solutions with different pH levels, including acidic (pH = 0), neutral (phosphate buffer solution, pH = 7.4), and basic (pH = 14), at room temperature. Fig. 9a. illustrates the average mass loss of S2 over time in various pH solutions, derived from triplicate experimental studies. The results indicate that S2 fully degraded in basic solution (100 %) over a period of 145 days, while it

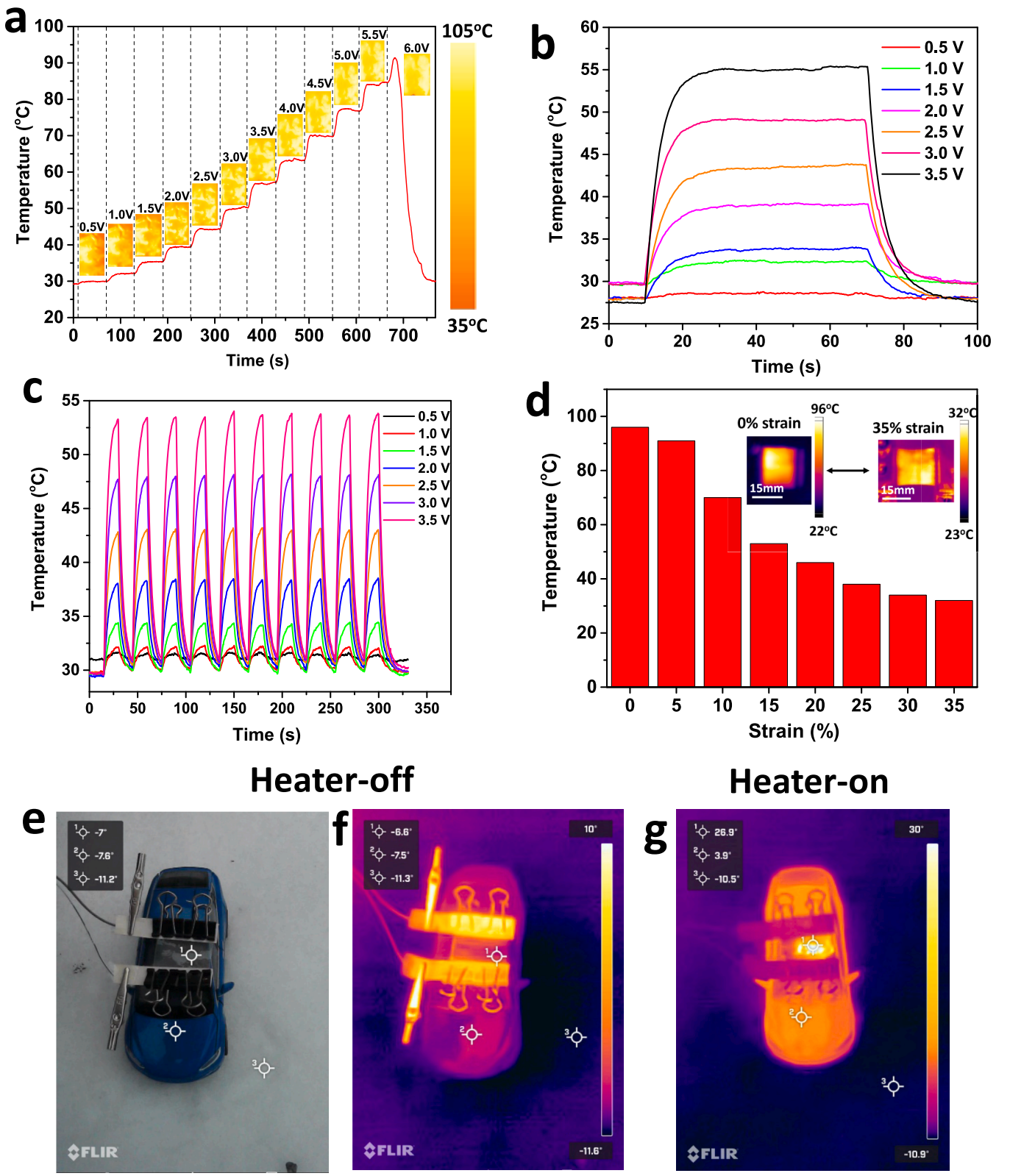

Fig. 8. Flexible heater characteristics and demonstration. (a) The heater shows a steady–state increase in heat with the stepwise increase of applied voltage from 0.5 V to 6 V. The corresponding IR images at different applied voltages show the uniform distribution of heat across the heater. (b) Time–dependent temperature profile of the heater at different applied voltages (0.5 V to 3.5 V) by turning the heater voltage on for 60 s. (c) The temperature response over heating cycles at different voltages (0.5 V to 3.5 V). (d) Temperature response over applied strains from 0-35 % at an applied bias of 5.5 V. (e–f) Camera and IR images of the TCE–based heater mounted on the windshield of a toy for defrosting in a cold environment under heater voltage–off conditions. (g) The IR image shows the even distribution of temperature across the heater surface mounted on a toy windshield when the heater is voltage–on.

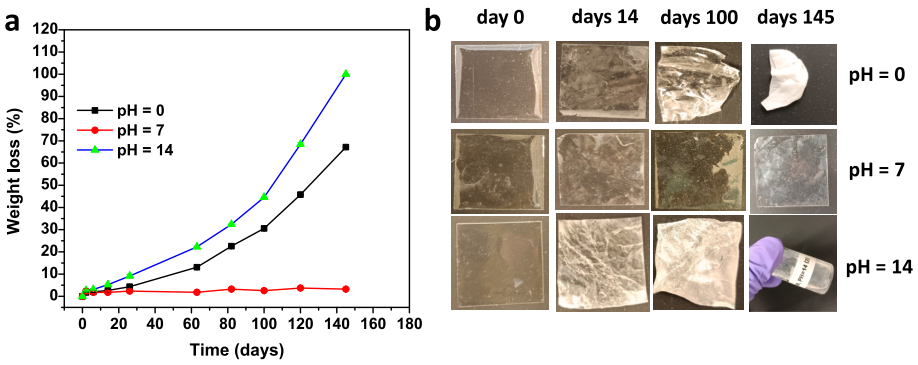

Fig.9. Degradability studies. (a) Weight loss percentage of S2 films show degradation over time under pH = 0, pH = 7.4 (phosphate buffer solution (PBS)), and pH = 14 solutions. (b) Images of thin films show degradation under various pH solutions at day 0, days 14, and days 145.

displayed notable mass loss in acidic solution (around 67 %) over the same period. In contrast, minimal mass loss (~3%) was observed for S2 in PBS over 145 days. Fig. 9b. demonstrates the morphological changes and degradation of polymer films under acidic, neutral, and basic solutions at days 14, 100, and 145, compared to the films at day 0 (initial films). The mass loss observed for polymer films under acidic and basic conditions can be due to accelerated cleavage of ester bonds catalyzed by H^+ and OH^- ions, respectively. Acid or base-catalyzed cleavage of esters is a well–known phenomenon for several degradable polyesters and their derivatives[37,65,66]. This phenomenon can lead to the breakdown of the S2 cross-linking network into their corresponding macromer or monomer fragments, resulting in a reduction of polymer molecular weights and subsequent mass loss. The possible mechanism for hydrolytic ester cleavage of S2 catalyzed by H^+ and OH^- ions is presented in scheme S1, supporting information. Based on the degradation studies, we conclude that polymer films are degradable and can be readily disposed of after serving their purpose as substrates in flexible devices.

It is noteworthy to mention that the poly(glycerol-*co*-δ-valerolactone) cyclohexyl urethane substrate can be considered as sustainable because its synthesis involves the use of degradable poly(glycerol-*co*-δ-valerolactone) triol, which is synthesized from renewable monomers such as glycerol and δ-valerolactone under solvent-free conditions [67–69]. literature survey suggested that the degraded products from these monomers are nontoxic and not potentially harmful to the environment[69], thus we have chosen them as starting monomers to prepare elastomers. Additionally, degradability studies show that our developed substrate demonstrates aquatic degradability under basic (100 % degradation at pH 14), acidic (67 % at pH 0), and neutral conditions (only 3 % degradation at pH 7.2 in PBS), making these substrates promising candidates for creating electronic waste (e-waste) free flexible devices. Additionally, very few degradable urethane-based elastomers are reported in the literature as sustainable substrates for flexible device applications [37–41], highlighting the importance of the sustainable substrates developed in this work for flexible devices.

4. Conclusion

In conclusion, we designed and synthesized sustainable substrates based on a new class of cross-linked poly(glycerol–*co*–δ–valerolactone) urethanes for stretchable electronic devices. The developed substrates display high flexibility, stretchability (~670 %), transparency (~90 %), thermal stability (~300 °C), and degradability. We developed stretchable, TCEs by using PVA nanofibers–based leveling technique and nano–welding Ag NWs, with uniform conductivity and low sheet resistance (~40 Ω sq^{-1} at 70 % transparency). These stretchable TCEs, along with versatile tactile sensors and thin–film heaters derived from them, demonstrate outstanding performance in wearables, human motion detection, and efficient heating in cold temperatures, offering a scalable and sustainable solution of substrates for advancing flexible electronics. As the cross-linked poly(glycerol–*co*–δ–valerolactone) urethanes are made up of renewable sustainable materials, it may help to reduce the carbon footprint and electronic waste. In addition, polymer films are eco–friendly, economical, easily accessible, easy to fabricate, and can be seamlessly integrated into the fabrication of next-generation stretchable devices. One shortcoming of the stretchable sensors and the heater demonstrated in our study is the lack of breathability that is sometimes required for wearables. This may be improved by simply electrospinning the polymers into nanofiber films. In the future, we hope to extend this work towards making these films breathable and integrating them with sustainable conductive parts such as conductive polymers or nanowires made of sustainable polymers.

CRediT authorship contribution statement

Pulikanti Guruprasad Reddy: Writing – review & editing, Writing – original draft, Supervision, Methodology, Formal analysis, Data curation, Conceptualization. **Amit Barua:** Validation, Methodology, Investigation, Formal analysis. **Timo Laukkanen:** Software, Formal analysis, Data curation. **Bahar Mostafiz:** Formal analysis, Data curation. **Teija Tirri:** Formal analysis, Data curation. **Akseli Vainio:** Visualization. **Vipul Sharma:** Writing – review & editing, Supervision, Resources, Project administration, Funding acquisition, Conceptualization.

Declaration of competing interest

The authors declare that they have no known competing financial interests or personal relationships that could have appeared to influence the work reported in this paper.

Data availability

Data will be made available on request.

Acknowledgments

This work is supported by financial support from KONE Foundation, the Research Council of Finland (grant no. 331368) and project DURATRANS (364364, 2024–2027, under the framework of M-ERA. Net). Authors are thankful to the Materials Research Infrastructure (MARI) at the University of Turku for infrastructural facilities.

Appendix A. Supplementary data

Supplementary data to this article can be found online at https://doi.org/10.1016/j.cej.2024.153531.

References

[1] S. Huang, Y. Liu, Y. Zhao, Z. Ren, C.F. Guo, Flexible Electronics: Stretchable Electrodes and Their Future, Adv. Funct. Mater. 29 (2019) 1805924, https://doi.org/10.1002/ADFM.201805924.

[2] M. Zarei, G. Lee, S.G. Lee, K. Cho, Advances in Biodegradable Electronic Skin: Material Progress and Recent Applications in Sensing, Robotics, and Human-Machine Interfaces, Adv. Mater. 35 (2023) 2203193, https://doi.org/10.1002/ADMA.202203193.

[3] W. Gao, H. Ota, D. Kiriya, K. Takei, A. Javey, Flexible Electronics toward Wearable Sensing, Acc Chem. Res. 52 (2019) 523–533, https://doi.org/10.1021/ACS.ACCOUNTS.8B00500.

[4] S. Chang, J.H. Koo, J. Yoo, M.S. Kim, M.K. Choi, D.H. Kim, Y.M. Song, Flexible and Stretchable Light-Emitting Diodes and Photodetectors for Human-Centric Optoelectronics, Chem. Rev. 124 (2024) 768–859, https://doi.org/10.1021/ACS.CHEMREV.3C00548.

[5] D. Won, J. Bang, S.H. Choi, K.R. Pyun, S. Jeong, Y. Lee, S.H. Ko, Transparent Electronics for Wearable Electronics Application, Chem. Rev. 123 (2023) 9982–10078, https://doi.org/10.1021/ACS.CHEMREV.3C00139.

[6] M. Fu, R. Lv, Y. Lei, M. Terrones, Ultralight flexible electrodes of nitrogen-doped carbon macrotube sponges for high-performance supercapacitors, Small 17 (2021) 2004827, https://doi.org/10.1002/SMLL.202004827.

[7] W. Li, S. Yang, W. Chen, J. Yang, H. Yu, R. Lv, M. Fu, Free-standing and flexible polyvinyl alcohol-sodium alginate-polypyrrole electrodes based on interpenetrating network hydrogels, J. Colloid. Interface. Sci. 664 (2024) 299–308, https://doi.org/10.1016/J.JCIS.2024.03.064.

[8] K. Jiang, S. Yang, W. Chen, K. Wang, M. Gao, L. Ning, R. Lv, H. Yu, M. Fu, Free-Standing $Co(OH)_2$/Prussian Blue Analogue Nanostructured Electrodes for Flexible Na-Ion Supercapacitors with an Ultrawide Potential Window, ACS. Appl. Nano. Mater. 7 (2024) 6650–6658, https://doi.org/10.1021/ACSANM.4C00603.

[9] X. Cui, F. Huang, X. Zhang, P. Song, H. Zheng, V. Chevali, H. Wang, Z. Xu, Flexible pressure sensors via engineering microstructures for wearable human-machine interaction and health monitoring applications, Iscience 25 (2022) 104148, https://doi.org/10.1016/J.ISCI.2022.104148.

[10] A. Mousavi, M. Rahimnejad, M. Azimzadeh, M. Akbari, H. Savoji, Recent advances in smart wearable sensors as electronic skin, J. Mater. Chem. B 11 (2023) 10332–10354, https://doi.org/10.1039/D3TB01373A.

[11] T. Sannicolo, M. Lagrange, A. Cabos, C. Celle, J.P. Simonato, D. Bellet, Metallic Nanowire-Based Transparent Electrodes for Next Generation Flexible Devices: a Review, Small 12 (2016) 6052–6075, https://doi.org/10.1002/SMLL.201602581.

[12] C. Wang, K. Xia, H. Wang, X. Liang, Z. Yin, Y. Zhang, Advanced Carbon for Flexible and Wearable Electronics, Adv. Mater. 31 (2019) 1801072, https://doi.org/10.1002/ADMA.201801072.

[13] S. Ryu, P. Lee, J.B. Chou, R. Xu, R. Zhao, A.J. Hart, S.G. Kim, Extremely Elastic Wearable Carbon Nanotube Fiber Strain Sensor for Monitoring of Human Motion, ACS Nano 9 (2015) 5929–5936, https://doi.org/10.1021/ACSNANO.5B00599.

[14] A.K. Katiyar, A.T. Hoang, D. Xu, J. Hong, B.J. Kim, S. Ji, J.H. Ahn, 2D Materials in Flexible Electronics: Recent Advances and Future Prospectives, Chem. Rev. 124 (2024) 318–419, https://doi.org/10.1021/ACS.CHEMREV.3C00302.

[15] X. Wu, W. Fu, H. Chen, Conductive Polymers for Flexible and Stretchable Organic Optoelectronic Applications, ACS Appl. Polym. Mater. 4 (2022) 4609–4623, https://doi.org/10.1021/ACSAPM.2C00519.

[16] D. Qi, Z. Liu, W.R. Leow, X. Chen, Elastic substrates for stretchable devices, MRS Bull 42 (2017) 103–107, https://doi.org/10.1557/MRS.2017.7.

[17] M. Hassan, G. Abbas, N. Li, A. Afzal, Z. Haider, S. Ahmed, X. Xu, C. Pan, Z. Peng, Significance of Flexible Substrates for Wearable and Implantable Devices: Recent Advances and Perspectives, Adv. Mater. Technol. 7 (2022) 2100773, https://doi.org/10.1002/ADMT.202100773.

[18] K.J. Baeg, J. Lee, Flexible Electronic Systems on Plastic Substrates and Textiles for Smart Wearable Technologies, Adv. Mater. Technol. 5 (2020) 2000071, https://doi.org/10.1002/ADMT.202000071.

[19] W.B. Han, J.H. Lee, J.W. Shin, S.W. Hwang, Advanced Materials and Systems for Biodegradable, Transient Electronics, Adv. Mater. 32 (2020) 2002211, https://doi.org/10.1002/ADMA.202002211.

[20] A. Singh Dahiya, A. Zumeit, A. Christou, R. Dahiya, A.S. Dahiya, A. Zumeit, A. Christou, R. Dahiya, High-Performance n-Channel Printed Transistors on Biodegradable Substrate for Transient Electronics, Adv. Electron. Mater. 8 (2022) 2200098, https://doi.org/10.1002/AELM.202200098.

[21] D. Baran, D. Corzo, G.T. Blazquez, Flexible Electronics: Status, Challenges and Opportunities, Front. Electron. 1 (2020) 594003, https://doi.org/10.3389/FELEC.2020.594003.

[22] W.B. Han, G.J. Ko, K.G. Lee, D. Kim, J.H. Lee, S.M. Yang, D.J. Kim, J.W. Shin, T.M. Jang, S. Han, H. Zhou, H. Kang, J.H. Lim, K. Rajaram, H. Cheng, Y.D. Park, S.H. Kim, S.W. Hwang, Ultra-stretchable and biodegradable elastomers for soft, transient electronics, Nat. Commun. 2023 14:1 14 (2023) 1–12, https://doi.org/10.1038/s41467-023-38040-4.

[23] Y. Yang, H. Zhao, Water-induced polymer swelling and its application in soft electronics, Appl. Surf. Sci. 577 (2022) 151895, https://doi.org/10.1016/J.APSUSC.2021.151895.

[24] Y. Jing, Z. Zhao, X. Cao, Q. Sun, Y. Yuan, T. Li, Ultraflexible, cost-effective and scalable polymer-based phase change composites via chemical cross-linking for wearable thermal management, Nat. Commun. 2023 14:1 14 (2023) 1–12, https://doi.org/10.1038/s41467-023-43772-4.

[25] J.C. Costa, F. Spina, P. Lugoda, L. Garcia-Garcia, D. Roggen, N. Münzenrieder, Flexible Sensors—From Materials to Applications, Technologies 7 (2019) 35, https://doi.org/10.3390/TECHNOLOGIES7020035.

[26] Y. Seo, B.S. Kim, W.C. Ballance, N. Aw, B. Sutton, H. Kong, Transparent and Flexible Electronics Assembled with Metallic Nanowire-Layered Nondrying Glycerogel, ACS. Appl. Mater, Interfaces 12 (2020) 13040–13050, https://doi.org/10.1021/ACSAMI.9B21697.

[27] M. Li, Y. Chen, Z. Kong, Z. Sun, L. Qian, Impact of a Novel Phosphoramide Flame Retardant on the Fire Behavior and Transparency of Thermoplastic Polyurethane Elastomers, ACS Omega 8 (2023) 18151–18164, https://doi.org/10.1021/ACSOMEGA.3C01464.

[28] Z. Hui, L. Zhang, G. Ren, G. Sun, H.D. Yu, W. Huang, Green Flexible Electronics: Natural Materials, Fabrication, and Applications, Adv. Mater. 35 (2023) 2211202, https://doi.org/10.1002/ADMA.202211202.

[29] L. Wang, K. Wang, Z. Lou, K. Jiang, G. Shen, Plant-Based Modular Building Blocks for "Green" Electronic Skins, Adv. Funct. Mater. 28 (2018) 1804510, https://doi.org/10.1002/ADFM.201804510.

[30] S.C. Teixeira, N.O. Gomes, T.V. de Oliveira, P. Fortes-Da-Silva, N. de F.F. Soares, P. A. Raymundo-Pereira, Review and Perspectives of sustainable, biodegradable, eco-friendly and flexible electronic devices and (Bio)sensors, Biosens Bioelectron X 14 (2023) 100371, https://doi.org/10.1016/J.BIOSX.2023.100371.

[31] H. Xiang, Z. Li, H. Liu, T. Chen, H. Zhou, W. Huang, Green flexible electronics based on starch, npj Flex, Electron. 6 (2022) 1–16, https://doi.org/10.1038/s41528-022-00147-x.

[32] T. Xing, A. He, Z. Huang, Y. Luo, Y. Zhang, M. Wang, Z. Shi, G. Ke, J. Bai, S. Zhao, F. Chen, W. Xu, Silk-based flexible electronics and smart wearable Textiles: Progress and beyond, Chem. Eng. J. 474 (2023) 145534, https://doi.org/10.1016/J.CEJ.2023.145534.

[33] I. Haider, M. Mosallaei, K. Yiannacou, A. Vehkaoja, S. Zakeri, V. Sariola, V. Sharma, Breathable, Flexible, Transparent, Hydrophobic, and Biotic Sustainable Electrodes for Heating and Biopotential Signal Measurement Applications, Adv. Eng. Mater. 25 (2023) 2201172, https://doi.org/10.1002/ADEM.202201172.

[34] A. Elsayes, V. Sharma, K. Yiannacou, A. Koivikko, A. Rasheed, V. Sariola, A. Elsayes, V. Sharma, K. Yiannacou, A. Koivikko, A. Rasheed, V. Sariola, Plant-Based Biodegradable Capacitive Tactile Pressure Sensor Using Flexible and Transparent Leaf Skeletons as Electrodes and Flower Petal as Dielectric Layer, Adv. Sustain. Syst. 4 (2020) 2000056, https://doi.org/10.1002/ADSU.202000056.

[35] V. Sharma, K. Jääskö, K. Yiannacou, A. Koivikko, V. Lampinen, V. Sariola, Performance Comparison of Fast, Transparent, and Biotic Heaters Based on Leaf Skeletons, Adv. Eng. Mater. 24 (2022) 2101625, https://doi.org/10.1002/ADEM.202101625.

[36] V. Sharma, A. Koivikko, K. Yiannacou, K. Lahtonen, V. Sariola, Flexible biodegradable transparent heaters based on fractal-like leaf skeletons, npj Flex, Electron. 4 (2020) 1–8, https://doi.org/10.1038/s41528-020-00091-8.

[37] S. Chen, Z. Wu, C. Chu, Y. Ni, R.E. Neisiany, Z. You, S. Chen, Z. Wu, C. Chu, Y. Ni, Z. You, R.E. Neisiany, Biodegradable Elastomers and Gels for Elastic Electronics, Adv. Sci. 9 (2022) 2105146, https://doi.org/10.1002/ADVS.202105146.

[38] Z. Yang, S. Zhang, Z. Chen, X. Lai, H. Li, X. Zeng, Self-Healing and Degradable Polycaprolactone-Based Polyurethane Elastomer for Flexible Stretchable Strain Sensors, ACS Appl. Polym. Mater. 6 (2024) 905–914, https://doi.org/10.1021/ACSAPM.3C02476.

[39] A.K. Brooks, S. Pradhan, V.K. Yadavalli, Degradable Elastomeric Silk Biomaterial for Flexible Bioelectronics, ACS Appl. Bio. Mater. 6 (2023) 4392–4402, https://doi.org/10.1021/ACSABM.3C00593.

[40] S. Chen, L. Sun, X. Zhou, Y. Guo, J. Song, S. Qian, Z. Liu, Q. Guan, E. Meade Jeffries, W. Liu, Y. Wang, C. He, Z. You, Mechanically and biologically skin-like elastomers for bio-integrated electronics, Nat. Commun. 11 (2020) 1–8, https://doi.org/10.1038/s41467-020-14446-2.

[41] L. Zhang, J. Liang, C. Jiang, Z. Liu, L. Sun, S. Chen, H. Xuan, D. Lei, Q. Guan, X. Ye, Z. You, Peptidoglycan-inspired autonomous ultrafast self-healing bio-friendly elastomers for bio-integrated electronics, Natl. Sci. Rev. 8 (2021) nwaa154, https://doi.org/10.1093/nsr/nwaa154.

[42] B.L. Turner, J. Twiddy, M.D. Wilkins, S. Ramesh, K.M. Kilgour, E. Domingos, O. Nasrallah, S. Menegatti, M.A. Daniele, Biodegradable elastomeric circuit boards from citric acid-based polyesters, npj Flex, Electron. 7 (2023) 1–14, https://doi.org/10.1038/s41528-023-00258-z.

[43] Texture Analysis Professionals Blog: Tensile Testing using a Texture Analyser – Calculating Fundamental Parameters, (n.d.). https://textureanalysisprofessionals.blogspot.com/2018/09/tensile-testing-using-texture-analyser.html.

[44] M.J.L. Tschan, E. Brulé, P. Haquette, C.M. Thomas, Synthesis of biodegradable polymers from renewable resources, Polym. Chem. 3 (2012) 836–851, https://doi.org/10.1039/C2PY00452F.

[45] E. Christodoulou, M. Notopoulou, E. Nakiou, M. Kostoglou, P. Barmpalexis, D. N. Bikiaris, Branched Poly(ε-caprolactone)-Based Copolyesters of Different Architectures and Their Use in the Preparation of Anticancer Drug-Loaded Nanoparticles, Int. J. Mol. Sci. 23 (2022) 15393, https://doi.org/10.3390/IJMS232315393/S1.

[46] L. Xue, S. Dai, Z. Li, Synthesis and characterization of three-arm poly(ε-caprolactone)-based poly(ester urethanes) with shape-memory effect at body temperature, Macromolecules 42 (2009) 964–972, https://doi.org/10.1021/MA802437F.

[47] S.L. Huang, J.Y. Lai, Structure-tensile properties of polyurethanes, Eur. Polym. J. 33 (1997) 1563–1567, https://doi.org/10.1016/S0014-3057(97)00058-X.

[48] N. Karna, G.M. Joshi, S.T. Mhaske, Structure-property relationship of silane-modified polyurethane: A review, Prog. Org. Coat. 176 (2023) 107377, https://doi.org/10.1016/J.PORGCOAT.2022.107377.

[49] B.N. Rao, P.U. Sastry, T. Jana, Structure-property relationships of ferrocene functionalized segmented polyurethane, Eur. Polym. J. 115 (2019) 201–211, https://doi.org/10.1016/J.EURPOLYMJ.2019.03.039.

[50] C. Lee, Y. Oh, I.S. Yoon, S.H. Kim, B.K. Ju, J.M. Hong, Flash-induced nanowelding of silver nanowire networks for transparent stretchable electrochromic devices, Sci. Rep. 8 (2018) 2763, https://doi.org/10.1038/s41598-018-20368-3.
[51] J. Miao, S. Chen, H. Liu, X. Zhang, Low-temperature nanowelding ultrathin silver nanowire sandwiched between polydopamine-functionalized graphene and conjugated polymer for highly stable and flexible transparent electrodes, Chem. Eng. J. 345 (2018) 260–270, https://doi.org/10.1016/J.CEJ.2018.03.144.
[52] X. Yu, X. Yu, J. Zhang, D. Zhang, J. Ni, H. Cai, D. Zhang, Y. Zhao, Investigation of light transmission and scattering properties in silver nanowire mesh transparent electrodes, Mater. Lett. 145 (2015) 219–223, https://doi.org/10.1016/J.MATLET.2015.01.025.
[53] H. Lee, M. Kim, I. Kim, H. Lee, Flexible and Stretchable Optoelectronic Devices using Silver Nanowires and Graphene, Adv. Mater. 28 (2016) 4541–4548, https://doi.org/10.1002/ADMA.201505559.
[54] D.C. Choo, W.K. Tae, Degradation mechanisms of silver nanowire electrodes under ultraviolet irradiation and heat treatment, Sci. Rep. 7 (2017) 1696, https://doi.org/10.1038/s41598-017-01843-9.
[55] V. Kalancha, A. These, L. Vogl, I. Levchuk, X. Zhou, M. Barr, M. Bruns, J. Bachmann, S. Virtanen, E. Spiecker, A. Osvet, C.J. Brabec, K. Forberich, Overcoming Temperature-Induced Degradation of Silver Nanowire Electrodes by an Ag@SnOx Core-Shell Approach, Adv. Electron. Mater. 8 (2022) 2100787, https://doi.org/10.1002/AELM.202100787.
[56] C.L. Kim, J.Y. Lee, D.G. Shin, J.S. Yeo, D.E. Kim, Mechanism of Heat-Induced Fusion of Silver Nanowires, Sci. Rep. 10 (2020) 9271, https://doi.org/10.1038/s41598-020-66304-2.
[57] Y.J. Fan, X. Li, S.Y. Kuang, L. Zhang, Y.H. Chen, L. Liu, K. Zhang, S.W. Ma, F. Liang, T. Wu, Z.L. Wang, G. Zhu, Highly Robust, Transparent, and Breathable Epidermal Electrode, ACS Nano 12 (2018) 9326–9332, https://doi.org/10.1021/ACSNANO.8B04245.
[58] D. Kim, S.H. Kim, J.H. Kim, J.C. Lee, J.P. Ahn, S.W. Kim, Failure criterion of silver nanowire electrodes on a polymer substrate for highly flexible devices, Sci. Rep. 7 (2017) 45903, https://doi.org/10.1038/srep45903.
[59] Y. Seo, H. Ha, P. Matteini, B. Hwang, A Review on the Deformation Behavior of Silver Nanowire Networks under Many Bending Cycles, Appl. Sci. 11 (2021) 4515, https://doi.org/10.3390/APP11104515.
[60] G. Yang, M.Z. Tian, P. Huang, Y.F. Fu, Y.Q. Li, Y.Q. Fu, X.Q. Wang, Y. Li, N. Hu, S. Y. Fu, Flexible pressure sensor with a tunable pressure-detecting range for various human motions, Carbon 173 (2021) 736–743, https://doi.org/10.1016/J.CARBON.2020.11.066.
[61] R. Li, Q. Zhou, Y. Bi, S. Cao, X. Xia, A. Yang, S. Li, X. Xiao, Research progress of flexible capacitive pressure sensor for sensitivity enhancement approaches, Sens. Actuators A Phys. 321 (2021) 112425, https://doi.org/10.1016/J.SNA.2020.112425.
[62] R.B. Mishra, N. El-Atab, A.M. Hussain, M.M. Hussain, Recent Progress on Flexible Capacitive Pressure Sensors: From Design and Materials to Applications, Adv. Mater. Technol. 6 (2021) 2001023, https://doi.org/10.1002/ADMT.202001023.
[63] T.Q. Trung, N.E. Lee, Flexible and Stretchable Physical Sensor Integrated Platforms for Wearable Human-Activity Monitoringand Personal Healthcare, Adv. Mater. 28 (2016) 4338–4372, https://doi.org/10.1002/ADMA.201504244.
[64] H. Wang, S. Li, H. Lu, M. Zhu, H. Liang, X. Wu, Y. Zhang, H. Wang, S. Li, H. Lu, M. Zhu, H. Liang, X. Wu, Y. Zhang, Carbon-Based Flexible Devices for Comprehensive Health Monitoring, Small Methods 7 (2023) 2201340, https://doi.org/10.1002/SMTD.202201340.
[65] J. Rydz, W. Sikorska, M. Kyulavska, D. Christova, Polyester-Based (Bio)degradable Polymers as Environmentally Friendly Materials for Sustainable Development, Int. J. Mol. Sci. 16 (2014) 564–596, https://doi.org/10.3390/IJMS16010564.
[66] P. Guruprasad Reddy, A.J. Domb, Formation of micro/nanoparticles and microspheres from polyesters by dispersion ring-opening polymerization, Polym. Adv. Technol. 32 (2021) 3835–3856, https://doi.org/10.1002/PAT.5476.
[67] A. Gandini, T.M. Lacerda, From monomers to polymers from renewable resources: Recent advances, Prog. Polym. Sci. 48 (2015) 1–39, https://doi.org/10.1016/J.PROGPOLYMSCI.2014.11.002.
[68] S. Luleburgaz, E. Cakmakci, H. Durmaz, U. Tunca, Sustainable polymers from renewable resources through click and multicomponent reactions, Eur. Polym. J. 209 (2024) 112897, https://doi.org/10.1016/J.EURPOLYMJ.2024.112897.
[69] M.A. Rasool, I.F.J. Vankelecom, Use of γ-valerolactone and glycerol derivatives as bio-based renewable solvents for membrane preparation, Green Chem. 21 (2019) 1054–1064, https://doi.org/10.1039/c8gc03652g.